

The effect of photometric redshift uncertainties on galaxy clustering and baryonic acoustic oscillations

Jonás Chaves-Montero^{1*}, Raúl E. Angulo², & Carlos Hernández-Monteagudo²

¹ *High Energy Physics Division, Argonne National Laboratory, Lemont, IL 60439, USA.*

² *Centro de Estudios de Física del Cosmos de Aragón, Plaza San Juan 1, Planta-3, 44001, Teruel, Spain.*

11 April 2018

ABSTRACT

In the upcoming era of high-precision galaxy surveys, it becomes necessary to understand the impact of redshift uncertainties on cosmological observables. In this paper we explore the effect of sub-percent photometric redshift errors (photo- z errors) on galaxy clustering and baryonic acoustic oscillations (BAO). Using analytic expressions and results from 1 000 N -body simulations, we show how photo- z errors modify the amplitude of moments of the 2D power spectrum, their variances, the amplitude of BAO, and the cosmological information in them. We find that: a) photo- z errors suppress the clustering on small scales, increasing the relative importance of shot noise, and thus reducing the interval of scales available for BAO analyses; b) photo- z errors decrease the smearing of BAO due to non-linear redshift-space distortions (RSD) by giving less weight to line-of-sight modes; and c) photo- z errors (and small-scale RSD) induce a scale dependence on the information encoded in the BAO scale, and that reduces the constraining power on the Hubble parameter. Using these findings, we propose a template that extracts unbiased cosmological information from samples with photo- z errors with respect to cases without them. Finally, we provide analytic expressions to forecast the precision in measuring the BAO scale, showing that spectro-photometric surveys will measure the expansion history of the Universe with a precision competitive to that of spectroscopic surveys.

Key words: large-scale structure of the Universe – distance scale – cosmological parameters – surveys – techniques: photometric – galaxies: distances and redshifts

1 INTRODUCTION

A new generation of wide-field cosmological galaxy surveys will soon map the spatial distribution of hundreds of millions of galaxies over a wide range of redshifts. With these, it will be possible to characterise the expansion history of the Universe and the growth of structures with exquisite precision. Moreover, these measurements will set strong constraints on the contributors to the total energy density as a function of redshift, the law of gravity on large scales, and perhaps will offer hints to explain the accelerated expansion of the Universe (see Weinberg et al. 2013, for a review).

Some of these future galaxy surveys will employ spectrographs, which will deliver precise estimates for galaxy redshifts, e.g. Dark Energy Spectroscopic Instrument (DESI, DESI Collaboration et al. 2016), WEAVE (Dalton et al. 2014), Euclid (Laureijs et al. 2011), and 4-metre Multi-Object Spectroscopic Telescope (4MOST, de Jong 2011). Other surveys, instead, will rely on either linear variable filters or sets of narrow-band filters, e.g. the Physics of the Accelerating Universe Survey (PAUS, Martí et al. 2014),

the Javalambre Physics of the accelerating universe Astrophysical Survey (J-PAS, Benitez et al. 2014), and the Spectro-Photometer for the History of the Universe, Epoch of Reionization, and Ices Explorer (SPHEREx, Doré et al. 2014, 2016). The advantages of the latter class are: higher surveying speeds, spectral data for every region of the sky, and a larger number of characterised objects. On the other hand, this approach adds non-negligible uncertainties to the measured redshifts, which propagates to the observed galaxy density field. In order to fully exploit the potential of this class of surveys, the effect of noisy redshift estimators on galaxy clustering has to be carefully studied.

The impact of photometric redshift errors (photo- z errors) on galaxy clustering and baryonic acoustic oscillations (BAO) has been investigated by several authors (e.g., Seo & Eisenstein 2003; Glazebrook & Blake 2005; Blake & Bridle 2005; Dolney et al. 2006; Seo & Eisenstein 2007; Cai et al. 2009; Benítez et al. 2009; Sereno et al. 2015; Ross et al. 2017). These studies have concluded that, in configuration space, adding photo- z errors to galaxy redshifts can be regarded as a smoothing of the galaxy density field along the line-of-sight (LOS). The analogous effect in Fourier space is a suppression of LOS k -modes. Despite this, these authors

* jchavesmontero@anl.gov

demonstrated that BAO can still be detected and used to measure the expansion history of the Universe through the Hubble parameter $H(z)$ and the angular diameter distance $D_A(z)$ (e.g., Seo & Eisenstein 2003). For instance, for the same number density, the uncertainty on the measured acoustic scale only doubles for photo- z errors of 0.3% with respect to a spectroscopic case (Cai et al. 2009).

In this paper we extend previous studies by developing a complete framework to extract cosmological information from BAO analyses under the presence of photo- z errors. In the first half of the manuscript, we explore the problem analytically. We provide expressions for power spectrum moments (related, but not identical, to Legendre multipoles) and their variances; we study the respective signal-to-noise ratios (SNR); and we quantify the cosmological information encoded in BAO, all this as a function on the photo- z errors and number density of a given sample. In addition, we provide a formula that forecasts the precision with which $H(z)$ and $D_A(z)$ can be measured, as function number density, linear bias, and typical photo- z uncertainty. In the second half of the paper, we use these results to build an unbiased estimator of the BAO scale from data with photo- z errors. We test the method by applying it to multiple samples drawn from a set of 1000 cosmological N -body simulations.

Our paper is organised as follows: in §2 we describe our cosmological simulations and how we compute clustering statistics and mimic photo- z errors. In §3 we derive analytic expressions for the impact of photo- z errors on power spectrum moments and their variances, which we compare with the results from our set of simulations. Then, in §4, we model how photo- z errors modify the suppression of BAO and the cosmological information that they encode. In §5 we build an unbiased model for extracting the contribution of BAO to power spectrum moments, and in §6 we apply it to simulated samples with different number densities and photo- z errors. In §7 we make forecasts for the precision with which cosmological parameters can be measured from galaxy surveys with sub-percent photo- z errors and in §8 we summarise our most important results.

2 NUMERICAL METHODS

In this section we present the numerical simulations that we analyse, we explain how we measure power spectrum moments and their respective variances, and we describe how we mimic photo- z errors in the simulations.

2.1 Numerical Simulations

Typically, numerical simulations poorly sample the modes where BAO are located (but see Angulo & Pontzen 2016). Additionally, owing to periodic boundary conditions, simulations do not consider the coupling with modes larger than the box size. To avoid these complications and obtain accurate results, it is necessary to consider ensembles of N -body simulations of volumes in excess of $1 h^{-3} \text{Gpc}^3$ when analysing the BAO feature (Angulo et al. 2008).

In this work we have carried out an ensemble of 1000 N -body simulations, where each of them evolved 1024^3 dark matter (DM) particles of mass $1.7 \times 10^{12} h^{-1} M_\odot$ in a cubic box of $3 h^{-1} \text{Gpc}$ on a side from different initial conditions. This suite has an aggregated volume of $27\,000 h^{-3} \text{Gpc}^3$, which will allow us to accurately resolve the BAO feature.

For computational efficiency, we carried out these simulations using the Comoving Lagrangian Acceleration (COLA) method (Tassev et al. 2013). This algorithm is able to recover the real-space power spectrum of a full N -body simulation to within 2% for $k < 0.3 h \text{Mpc}^{-1}$ at a fraction of its computational cost (Howlett et al. 2015). Moreover, COLA reproduces the redshift-space power spectrum monopole and quadrupole of HOD galaxies for $k < 0.2 h \text{Mpc}^{-1}$ (Koda et al. 2016).

We adopt Gaussian initial conditions created using 2nd-order Lagrangian Perturbation theory. Gravitational forces were computed using a Particle-Mesh algorithm with a Fourier grid of 1024^3 points, and particles were evolved from $z = 9$ down to $z = 1$ in 10 time steps. The cosmological parameters adopted were $\Omega_m = 0.25$, $\Omega_\Lambda = 0.75$, $\Omega_b = 0.045$, $n_s = 1$, $H_0 = 73 \text{ km s}^{-1} \text{Mpc}^{-1}$, and $\sigma_8 = 0.9$. Each simulation took 3 CPU hours to complete.

The COLA ensemble will allow us to investigate the impact of photo- z errors on power spectrum moments, their variances, and BAO. We will only explore the $z = 1$ outputs, which is motivated by the target redshift of future surveys, but our results can be readily generalised to any redshift and for a full lightcone. In addition, we will only focus on dark matter statistics, since the typical number density of halos that can be resolved with at least 100 particles in our simulations, $n = 1.17 \times 10^{-6} h^3 \text{Mpc}^{-3}$, is too low for clustering studies (thus BAO scales are dominated by shot noise). Nevertheless, extrapolating our results to biased tracers can be done by considering the adequate number density and fluctuations amplitude.

2.2 Power spectrum and covariance measurements

Throughout this paper we study the matter density field in Fourier space using its power spectrum, $P(\mathbf{k})$, defined by

$$\langle \hat{\delta}(\mathbf{k}) \hat{\delta}(\mathbf{k}') \rangle = (2\pi)^3 \delta_{\text{D}}(\mathbf{k} - \mathbf{k}') P(\mathbf{k}), \quad (1)$$

where $\langle \rangle$ indicates an ensemble average, $\delta_{\text{D}}()$ is the Dirac delta function, and $\hat{\delta}(\mathbf{k})$ is the Fourier transform of the density contrast field, $\delta(\mathbf{x})$. Operationally, we compute $P(\mathbf{k})$ by gridding the DM particles of each simulation onto a 1024^3 cubic lattice using a cloud-in-cell (CIC) scheme (Hockney & Eastwood 1981). Then, we Fast Fourier Transform this field and correct for the assignment scheme by dividing by the Fourier transform of the CIC window function. We expect this to provide power spectrum estimates accurate to within 0.1% up to $k = 0.4 h \text{Mpc}^{-1}$ (Sefusatti et al. 2016).

Within the plane-parallel approximation, the 3D power spectrum has an azimuthal symmetry and it can be decomposed in terms of the following moments:

$$P_\ell(k) = \frac{1}{2} \int_{-1}^1 d\mu \mu^\ell P(k, \mu), \quad (2)$$

where $k \equiv |\mathbf{k}|$ is the modulus of the wave-vector \mathbf{k} , and $\mu = \frac{\mathbf{k} \cdot \hat{\mathbf{z}}}{k}$.

In the Kaiser approximation, the full 2D power spectrum can be written using combinations of $\ell = 0, 2$, and 4 moments only. Even when considering nonlinearities, almost all cosmological information is encoded in these three moments, which is why we will only consider these in our subsequent analysis.

Note that we chose to adopt moments of the power spectrum, rather than the more common Legendre multipoles, for

simplicity in the analytic expressions and in the numerical analysis we will present later. In practice, this choice is unimportant as any Legendre multipole of order ℓ' can be written as a linear combination of moments of order $\ell \leq \ell'$.

To minimise the impact of a discrete sampling of wavemodes, specially on large scales, we compute $P_\ell(k)$ using a o -point Gauss-Legendre quadrature algorithm (Abramowitz & Stegun 1972; Szapudi et al. 2001; Kashlinsky et al. 2001):

$$P_\ell(k) \simeq \frac{1}{2} \sum_i^o w_i y_i^\ell \hat{P}(k, y_i), \quad (3)$$

where $w_i = \frac{2}{(1-y_i^2)[\mathcal{L}'_o]^2}$ is a Gauss-Legendre weight, \mathcal{L}_o is the o -th order Legendre polynomial, and y_j is the j -root of the Legendre polynomial of order o . We estimate $\hat{P}(k, y)$ from neighbouring measurements:

$$\hat{P}(k, y) = \frac{\sum_{\mathbf{k}_i} \sum_j^o p(\mu_i, y_j) P(\mathbf{k}_i)^2}{\sum_{\mathbf{k}_i} \sum_j^o p(\mu_i, y_j)}, \quad (4)$$

where μ_i is the direct cosine of \mathbf{k}_i , and the sum $\sum_{\mathbf{k}_i}$ runs over the N_k wave-vectors \mathbf{k}_i that lie within a bin in k , which we define to be equally spaced in $\Delta k = (2\pi/L_{\text{box}})h \text{ Mpc}^{-1}$. The terms $p(\mu_i, y_j) = e^{-0.5(\mu_i - y_j)^2 / (\Delta p_j)^2}$ are arbitrary weights, which we set by choosing Δp_j to be twice the distance between two consecutive roots, $\Delta p_j = 2(y_{j+1} - y_j)$. We have checked that $o = 16$ is enough for accurate results. We note that on very large scales this algorithm introduces a small covariance between different μ -bins, owing to the limited number of available k -modes.

Finally, we apply a correction to every moment to remove at first order the contribution of shot noise, $P_\ell \rightarrow P_\ell - n^{-1}/(\ell + 1)$, where n is the average number density of objects considered.

An ensemble of M measurements can be used to compute the respective covariance matrix:

$$\mathbf{C}_\ell(k_i, k_j) = \frac{1}{M-1} \sum_{m=1}^M [P_\ell^m(k_i) - \bar{P}_\ell(k_i)][P_\ell^m(k_j) - \bar{P}_\ell(k_j)], \quad (5)$$

where P_ℓ^m is the ℓ -th moment of the m -th simulation and \bar{P}_ℓ its average estimated from M simulations. In §6 we will extract the BAO scale jointly from P_0 , P_2 , and P_4 . In that case, we substitute the vector P_ℓ^m by $\{P_0^m, P_2^m, P_4^m\}^T$.

We calculate the precision matrix, \mathbf{C}_ℓ^{-1} , by inverting the covariance matrix, $\tilde{\mathbf{C}}_\ell^{-1}$, using an algorithm based on a LU factorisation. The expected value of this matrix is biased when computed from a finite number of realisations. We correct for this as follows:

$$\mathbf{C}_\ell^{-1} = \frac{M - N_{\text{bins}} - 2}{M - 1} \tilde{\mathbf{C}}_\ell^{-1}, \quad (6)$$

where N_{bins} is the number of k -bins in P_ℓ (Hartlap et al. 2007).

2.3 Redshift uncertainties

We model redshift-space distortions (RSD) and photo- z errors in our simulations in the flat sky approximation, i.e. we perturb the comoving position of objects along the $\hat{\mathbf{k}}_z$ direction:

$$s_z = r_z + (1 + z_{\text{box}}) \frac{v_z}{H(z_{\text{box}})} + \delta(r_z) \quad (7)$$

where s_z and r_z are the perturbed and unperturbed comoving positions, respectively, v_z is the physical peculiar velocity along the z -axis in km s^{-1} , $H(z_{\text{box}})$ the Hubble parameter at the redshift of the simulation box in $\text{km s}^{-1} \text{Mpc}^{-1}$, and $\delta(r_z)$ a random variable that account for photo- z errors and whose PDF given by $\text{Pr}[\delta(r_z)]$.

Unless stated otherwise, in what follows we assume that $\text{Pr}[\delta(r_z)]$ is a Gaussian distribution with zero mean and standard deviation $\sigma = \sigma_z(1 + z_{\text{box}})cH^{-1}(z_{\text{box}})$ where σ_z indicates the precision in redshift.

3 EFFECT OF PHOTOMETRIC REDSHIFT ERRORS ON POWER SPECTRUM MOMENTS

In this section we derive analytic expressions for the impact of photo- z errors on power spectrum moments and their variances. In all cases, we compare these predictions with numerical results obtained from the COLA ensemble.

3.1 Power spectrum moments

3.1.1 General expressions

Let us consider a set of galaxies with a real-space overdensity $\hat{\delta}_r(\mathbf{k})$ discretely sampling a field of covariance $P(\mathbf{k})$, and whose redshifts are measured through a noisy but unbiased estimator. The observed redshifts are thus $z + \delta z$, where δz is the photo- z error. Assuming that the PDF of the photo- z errors, $\text{Pr}[\delta r_z]$, is identical for every galaxy, the redshift-space overdensity field within the Gaussian dispersion model (Kaiser 1987; Peacock & Dodds 1994) is:

$$\hat{\delta}_z(k, \mu) = \hat{\delta}_r(k) \mathcal{F}(k, \mu), \quad (8)$$

$$\mathcal{F}(k, \mu) \equiv (1 + \beta\mu^2) e^{-0.5[k\mu\sigma_v(1+z)/H(z)]^2} F(k\mu), \quad (9)$$

where $\beta \equiv b^{-1} d \ln D(a) / d \ln a$, b is the large-scale bias of the sample, $D(a)$ is the linear growth factor for dark matter, $a = (1 + z)^{-1}$ is the cosmological scale factor, σ_v is a velocity dispersion induced by non-linear dynamics in units of the speed of light, and $F(k\mu)$ is the Fourier transform of $\text{Pr}[\delta r_z]$. The first and second term of the RHS of Eq. 9 encode large- and small-scale RSD generated by the peculiar velocity of the galaxies, respectively, and the third the effect of photo- z errors. Hereafter, for brevity we will not write explicitly the dependence of $\mathcal{F}(k, \mu)$ on μ and k .

We have chosen to adopt a Gaussian form for distribution of small-scale velocities. However, other forms better fit the distributions measured in cosmological simulations (Scoccimarro 2004; Orsi & Angulo 2017). Our results can be easily generalised to those distributions by replacing the exponential term in Eq. 9 by the desired velocity distribution function.

From Eqs. 2,8, and 9, we can derive the relation between

power spectrum moments in redshift space, P_ℓ , and the $l = 0$ moment of the real-space power spectrum, P_0^r :

$$P_\ell(k) = \langle \mu^\ell \mathcal{F}^2 \rangle_{\mathbf{k}} P_0^r(k), \quad (10)$$

$$\langle \mu^\ell \mathcal{F}^2 \rangle_{\mathbf{k}} = \frac{1}{2} \int_{-1}^1 d\mu \mu^\ell \mathcal{F}^2, \quad (11)$$

where, here and in the remainder of this paper, the $\langle \dots \rangle_{\mathbf{k}}$ brackets denote an angular average.

3.1.2 The Gaussian case

For a Gaussian $\text{Pr}[\delta r_z]$, $F(k\mu) = \exp\{-0.5[k\mu\sigma_z(1+z)c/H(z)]^2\}$, and the $\ell = 0, 2$, and 4 moments can be derived analytically:

$$\langle \mathcal{F}^2 \rangle_{\mathbf{k}} = \frac{\sqrt{\pi} \text{Erf}(x)}{2} \frac{1}{x} \left(1 + \frac{\beta}{x^2} + \frac{3\beta^2}{4x^4} \right) - \frac{\beta e^{-x^2}}{x^2} \left(1 + \frac{3\beta}{4x^2} \mathcal{H}_1(x) \right), \quad (12)$$

$$\langle \mu^2 \mathcal{F}^2 \rangle_{\mathbf{k}} = \frac{\sqrt{\pi} \text{Erf}(x)}{4} \frac{1}{x^3} \left(1 + \frac{3\beta}{x^2} + \frac{15\beta^2}{4x^4} \right) - \frac{e^{-x^2}}{2x^2} \left(1 + \frac{3\beta}{x^2} \mathcal{H}_1(x) + \frac{15\beta^2}{4x^4} \mathcal{H}_2(x) \right), \quad (13)$$

$$\langle \mu^4 \mathcal{F}^2 \rangle_{\mathbf{k}} = \frac{3\sqrt{\pi} \text{Erf}(x)}{8} \frac{1}{x^5} \left(1 + \frac{5\beta}{x^2} + \frac{35\beta^2}{4x^4} \right) - \frac{3e^{-x^2}}{4x^4} \left(\mathcal{H}_1(x) + \frac{5\beta}{x^2} \mathcal{H}_2(x) + \frac{35\beta^2}{4x^4} \mathcal{H}_3(x) \right), \quad (14)$$

where $\mathcal{H}_n(x) = \sum_{i=0}^n \frac{2^i}{(2i+1)!!} x^{2i}$, !! denotes the double factorial, $x = k\sigma_{\text{eff}}$, and $\sigma_{\text{eff}} = \sqrt{\sigma_z^2 + \sigma_v^2} (1+z)c/H(z)$, i.e. the redshift uncertainties and small-scale peculiar velocities are added in quadrature (Peacock & Dodds 1994). Note that these expressions diverge as $x \rightarrow 0$, and in general $\langle \mu^n \mathcal{F}^m \rangle_{\mathbf{k}}$ expressions are only valid when $x > 3$. To obtain valid expressions when $x < 3$, we expand $F(k\mu)$ into a power series.

The expressions in real space can be trivially obtained by setting $\beta = 0$ and $\sigma_{\text{eff}} = \sigma$, recovering the expression for Eq. 12 provided in Peacock & Dodds (1994). In that case, we can see that photo- z errors always generates an apparent anisotropic clustering, even if the underlying galaxy field is isotropic. In redshift space the effect is more complex as photo- z errors couple with RSD parameters. We will explore this next.

3.1.3 Comparison with numerical simulations

In the top panels of Fig. 1 we display the average power spectrum moments from our analytic expression and from the COLA ensemble. Symbols and colours indicate the results for samples with different number densities and photo- z errors, as stated in the legend. To compute our model, we employ the average P_0^r from the COLA ensemble with $n = 0.03 h^3 \text{Mpc}^{-3}$ and $\sigma_v = 3 \times 10^{-4}$, where σ_v is obtained by fitting our analytic model to power spectrum moments of samples without photo- z errors.

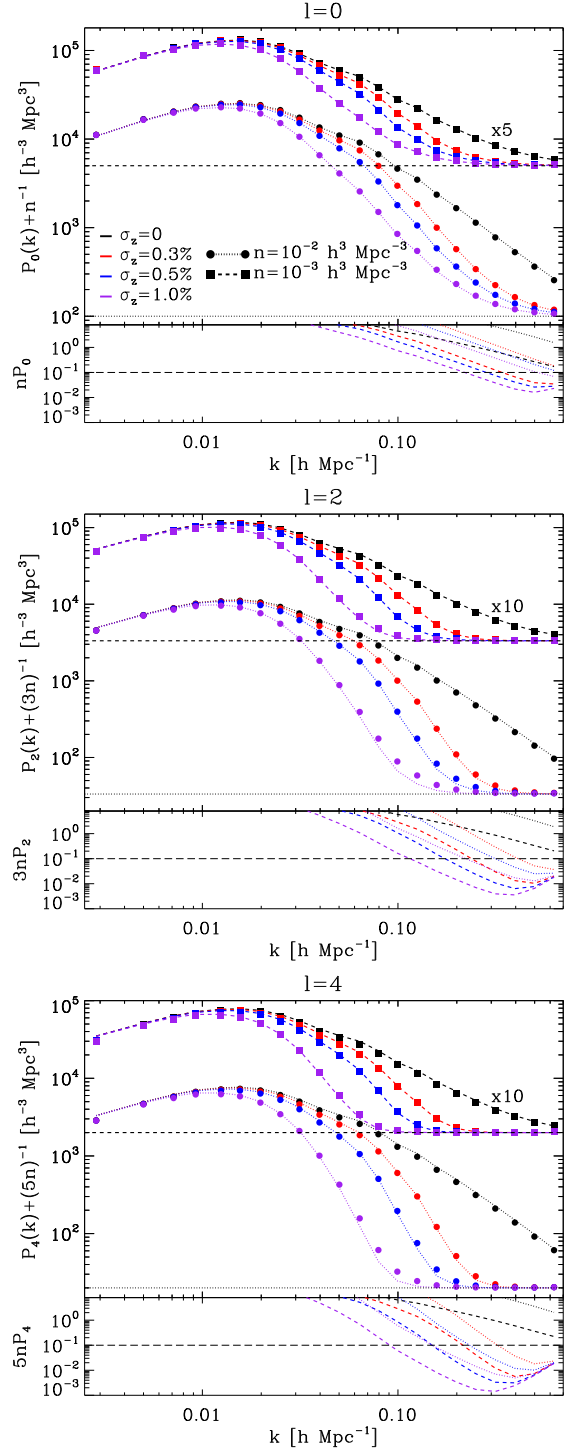


Figure 1. **Top panels:** impact of photo- z errors on P_0 , P_2 , and P_4 . Symbols show the average results from an ensemble of 1000 N -body simulations and lines our analytic predictions (Eqs. 10–14), which employ as input the average P_0^r from simulations with $n = 0.03 h^3 \text{Mpc}^{-3}$ and $\sigma_v = 3 \times 10^{-4}$. The colour and shape of lines and symbols indicate the size of Gaussian photo- z errors and the number density for each sample, respectively, as stated in the legend. Results for different number densities are vertically displaced for clarity. We employ this colour-coding in what follows. Horizontal lines indicate the shot noise level. Our analytic model precisely captures the effect of photo- z errors. **Bottom panels:** ratio of shot noise corrected power spectrum moments from simulations and shot noise. On the scales where $(2\ell + 1)nP_\ell < 0.1$ (indicated by long-dashed lines) the shot noise correction is no longer accurate.

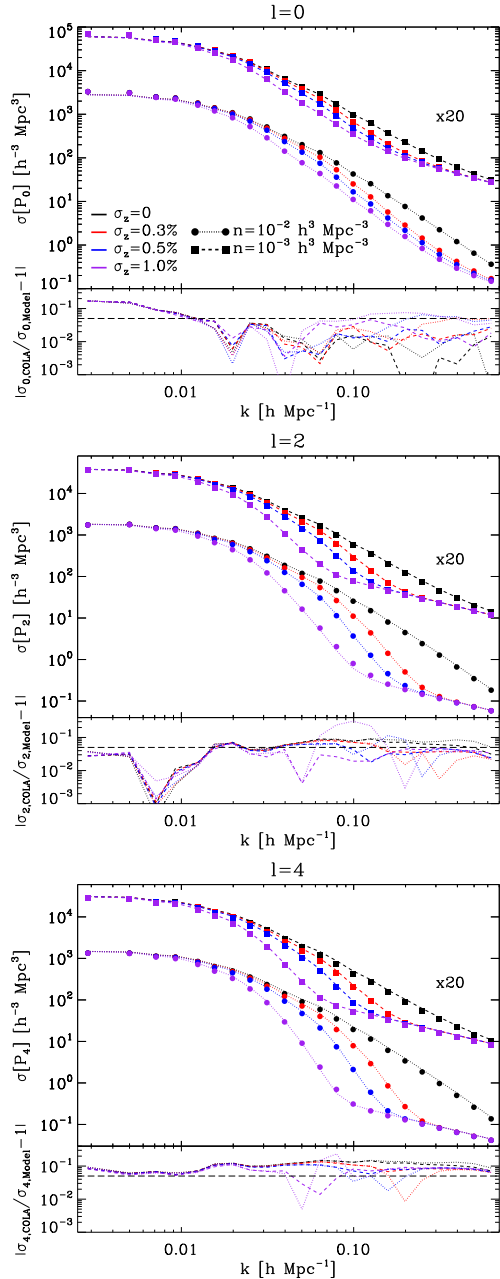


Figure 2. The impact of photometric errors on the variance of the moments of the redshift-space power spectrum. In each panel we show three sets of curves displaying the results for different number densities. Within each set, colours indicate different redshift uncertainties, as indicated by the legend. Symbols indicate the mean values from our ensemble of simulations, whereas dotted lines indicate the analytic model of Eqs. 16. The bottom panel of each figure shows the fractional difference between our numerical and analytic results.

We can see that our numerical and analytical results show good agreement. The discrepancies, of the order of 10%, arise from the inaccuracy of our RSD model and shot noise subtraction. In the bottom panels of Fig. 1 we display the ratio of shot noise corrected moments and their shot noise level. The long dashed line indicates when the shot noise level is 10 times greater than the amplitude of shot noise corrected moments. As we can see, below this line the shot noise subtraction is no longer precise.

Overall, we can see that photo- z errors suppress the amplitude of P_0 , P_2 , and P_4 for all wavenumbers, specially on small scales. The Poisson noise, however, is unaltered. Therefore, for a given number density of objects, photo- z s reduce the number of modes and scales useful for cosmological analyses. This is the main effect for galaxy clustering.

3.2 Variance of power spectrum moments

3.2.1 General expressions

The effect of photo- z errors is not only to modify the amplitude of the power spectrum P but also its Gaussian covariance. Let us first consider the diagonal elements of the power spectrum covariance matrix:

$$\sigma^2[P](k) = \frac{2}{N_k} \sum_{\mathbf{k}_i} \langle |\hat{\delta}(\mathbf{k}_i)|^4 \rangle - \langle \hat{P}(\mathbf{k}_i) \rangle^2, \quad (15)$$

where $\langle \dots \rangle$ denotes the ensemble average over multiple realisations/universes. The factor two appears because only half of the modes of the power spectrum are independent due to the reality of $\delta(\mathbf{x})$.

Assuming that the real and imaginary parts of $\hat{\delta}(\mathbf{k})$ are Gaussian random variables with zero mean and standard deviation $P/2$, and combining Eqs. 10 and 15, we obtain the following expression for the variance of power spectrum moments in redshift space under the presence of shot noise, photo- z errors, and small-scale velocities:

$$\sigma^2[P_\ell] = \frac{2}{N_k} \left[\langle \mu^{2\ell} \mathcal{F}^4 \rangle_{\mathbf{k}} + \frac{2 \langle \mu^{2\ell} \mathcal{F}^2 \rangle_{\mathbf{k}}}{nP_0^r} + \frac{1}{(2\ell + 1)(nP_0^r)^2} \right] (P_0^r)^2, \quad (16)$$

where this expression reduces to that provided by Colombi et al. (2009) for $\ell = 0$ in real space without photo- z errors ($\mathcal{F} = 1$). Note that to compute the diagonal terms of the covariance between two power spectrum moments P_ℓ and $P_{\ell'}$, we only have to substitute 2ℓ by $\ell + \ell'$ in the previous equation.

Note that for a Gaussian $\text{Pr}[\delta r_z]$, all terms in Eq.16 have an analytic expression, which we provided in §3.1.2. We can thus analytically compute the variance of any power spectrum moment.

3.2.2 Comparison with simulations: diagonal terms

In Fig. 2 we display the variance of P_0 , P_2 , and P_4 for the same samples shown in Fig. 1. In the bottom panels we compare our analytic model and the results from our simulations. Overall, our expressions correctly capture the effect of photo- z s – the agreement is to within 5%, 10%, and 20% for P_0 , P_2 , and P_4 , respectively. The differences originate from assuming that the matter density field is Gaussian, and thus from neglecting in our calculations the contribution of a non-zero trispectrum.

We see that photo- z errors reduce the variance, especially on intermediate scales where BAO are located, which is analogous to their effect on the amplitude of power spectrum moments. On the other hand, at a fixed scale, the contribution of shot noise progressively dominates as the order of the moment increases. We can understand this from 16: since the last term in brackets of Eq. does not depend on photo- z errors, it will be more important as the redshift uncertainty increases.

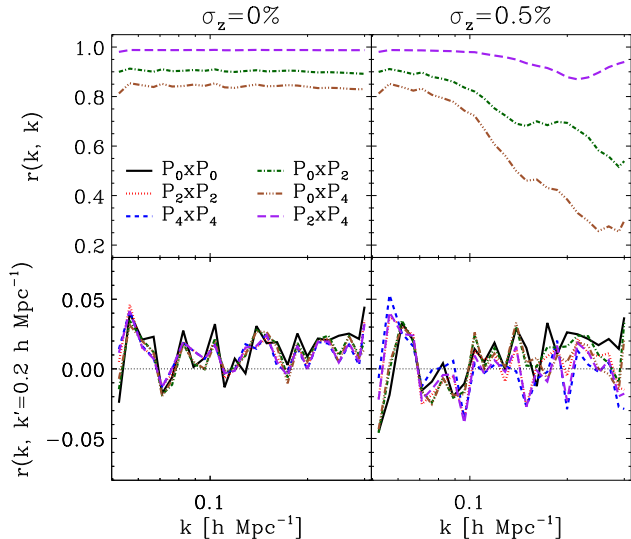


Figure 3. Diagonal and off-diagonal elements (top and bottom panels, respectively) of the auto-correlation matrices of P_0 , P_2 , P_4 , and their cross-correlations. The left and right panels show the results for $\sigma_z = 0$ and 0.5% , respectively, which are computed using 1000 samples from the COLA ensemble with $n = 0.01 h^3 \text{Mpc}^{-3}$. For samples with photo- z errors the diagonal terms of the cross-correlations decrease on small scales (we do not display those of the auto-correlations because their value is one by definition). Off-diagonal terms are computed at $k = 0.2 h \text{Mpc}^{-1}$, and their amplitudes are small independently of the size of photo- z errors.

3.2.3 Comparison with simulations: off-diagonal terms

In Fig. 3 we display the diagonal and off-diagonal elements of the auto-correlation matrices of P_0 , P_2 , and P_4 , and their cross-correlations for $\sigma_z = 0$ and 0.5% . The results shown are computed using 1000 samples from the COLA ensemble with $n = 0.01 h^3 \text{Mpc}^{-3}$. The top panels display the cross-correlation between different moments, which is scale-independent for samples with no errors. However, for samples with photo- z errors they decrease by increasing the value of k . This is the consequence of photo- z errors modifying the information content of power spectrum moments, we further analyse this in the following section.

On the bottom panels we display the off-diagonal terms of the correlation matrices at $k = 0.2 h \text{Mpc}^{-1}$. They are negligible at this scale for samples with and without photo- z errors. This is because photo- z errors do not modify the structure of the covariance matrix. In particular, in the plane-parallel approximation if the real-space power spectrum covariance matrix is diagonal for samples with no photo- z errors, then so it is in redshift space with or without photo- z errors. We check that in the whole range of scales used for BAO analyses in §6 off-diagonal are also smaller than 5% , which will justify the employment of Eq. 33. Nonetheless, on even smaller scales the covariance matrix is no longer diagonal due to non-linearities.

3.3 Signal-to-noise ratio

Let us now consider the SNR of power spectrum moments, which we define as the ratio between a given moment and the square root of its variance. We use this approximation because the covariance matrices of P_0 , P_2 , and P_4 are mostly diagonal on the scales where BAO are located, as we showed

in the previous section. Photo- z errors decrease the amplitude of power spectrum moments as well as their variances, and thus the resulting SNR will depend on a balance between both effects.

3.3.1 Toy model

In this subsection we introduce a toy model to understand how photo- z errors modify the SNR of P_0 , where it is straightforward to extend this model to $\ell > 0$. The model is the following:

$$\hat{P}_0 = \frac{1}{2} \hat{P}_0^r \left[\eta(\mu_1) e^{-k^2 \sigma_{\text{eff}}^2 \mu_1^2} + \eta(\mu_2) e^{-k^2 \sigma_{\text{eff}}^2 \mu_2^2} \right], \quad (17)$$

where the terms in brackets provide the angular contribution at only two μ -values (μ_1 and μ_2), the symbol \hat{P}_0^r denotes the measured real-space $\ell = 0$ moment, and $\eta(\mu)$ describes the contribution of large-scale RSD in a μ -bin. We will assume that $\mu_1 < \mu_2$, and thus $\eta(\mu_1) < \eta(\mu_2)$ since on linear scales $\eta(\mu)$ is a monotonically increasing function of μ .

For an ensemble average over a given k -bin we have that the SNR per radial k -interval reads:

$$\text{SNR} = \frac{1 + \eta_{21} \exp(-k^2 \sigma_{\text{eff}}^2 \Delta\mu^2)}{\sqrt{1 + \eta_{21}^2 \exp(-2k^2 \sigma_{\text{eff}}^2 \Delta\mu^2)}}, \quad (18)$$

with $\Delta\mu^2 = \mu_2^2 - \mu_1^2$ and $\eta_{21} = \eta(\mu_2)/\eta(\mu_1)$. From this expression, we shall consider three different cases:

- No photo- z errors nor small-scale RSD, $k \sigma_{\text{eff}} = 0$. In this case

$$\text{SNR} = \frac{1 + \eta_{21}}{\sqrt{1 + \eta_{21}^2}}, \quad (19)$$

where the SNR is always below $\sqrt{2}$, which is the value corresponding to real space.

- Very large photo- z errors, $k \sigma_{\text{eff}} \rightarrow \infty$. In this limit, the value of the SNR is 1. It is smaller than in the first case because all information along k -modes parallel to the LOS is lost.

- Small photo- z errors, $k \sigma_{\text{eff}} \rightarrow 0$. In this case, to first order in $(k \sigma_{\text{eff}})^2$ we obtain

$$\text{SNR} = \frac{1 + \eta_{21}}{\sqrt{1 + \eta_{21}^2}} + \frac{\Delta\mu^2 \eta_{21} (\eta_{21} - 1)}{(1 + \eta_{21}^2)^{3/2}} (k \sigma_{\text{eff}})^2 + \mathcal{O}[(k \sigma_{\text{eff}})^4], \quad (20)$$

where in this limit the SNR increases with respect to the case without photo- z errors nor small-scale RSD as $\eta_{21} > 1$. This behaviour must thus yield a local maximum in the SNR, since for larger $k \sigma_{\text{eff}}$ values we must recover the second case. This reflects that in this limit photo- z errors affect more the standard deviation of P_0 than its amplitude, and thus they slightly increase the SNR.

From Eq. 18 we find that the scale corresponding to the local maximum of the SNR, $\partial(\text{SNR})/\partial(k \sigma_{\text{eff}})^2 = 0$, is $(k \sigma_{\text{eff}})^2 = \ln(\eta_{21})/\Delta\mu^2$. That is $(k \sigma_{\text{eff}})^2 \simeq 1$, as shown in the top panel of Fig. 4.

3.3.2 Comparison with simulations

We now compare our analytic expressions for the SNR of power spectrum moments (i.e. those derived in the previous

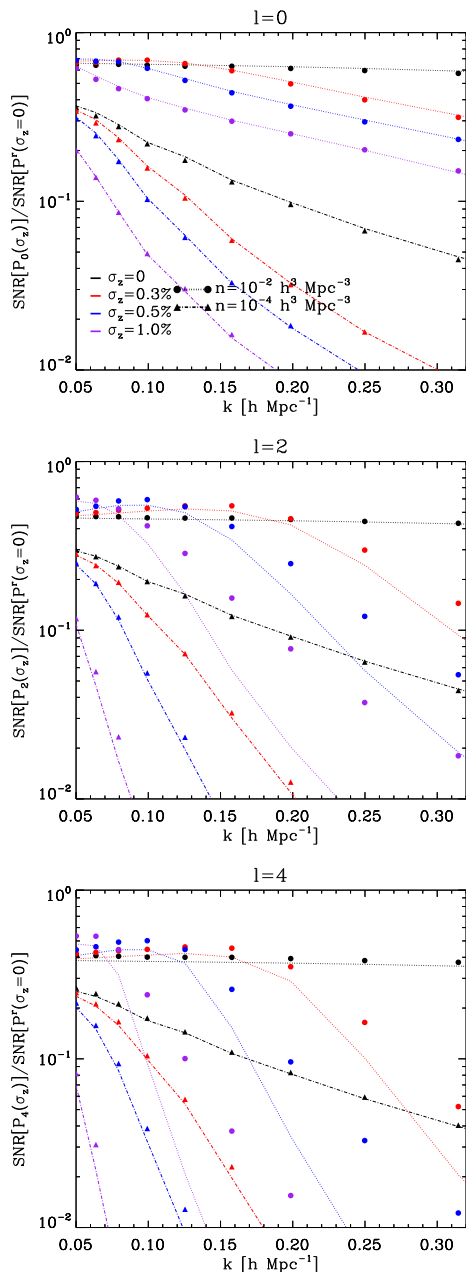


Figure 4. Ratio of the SNR of power spectrum moments, $P_\ell/\sigma[P_\ell]$, to that of a case with no photo- z errors and $n = 0.03 h^3 \text{Mpc}^{-3}$ in real space, $P^r/\sigma[P^r]$. On large scales, the SNR of P_ℓ is greater for samples with large number densities and photo- z errors. However, on small scales the SNR of power spectrum moments decreases by increasing σ_z .

two subsections) with the results from the COLA ensemble. In Fig. 4 we show the SNR of P_0 , P_2 , and P_4 relative to that of the real-space power spectrum with $n = 0.03 h^3 \text{Mpc}^{-3}$ and no photo- z errors. We present the redshift-space results for two number densities, as indicated by the legend. In all cases we can see that our model, indicated by lines, approximately reproduces the numerical data, displayed by symbols. The differences for $n = 10^{-2} h^3 \text{Mpc}^{-3}$ on large scales are driven by our model for the shot noise subtraction. Independently of the size of photo- z errors, on large scales the SNR of each moment is lower than that of the real-space power spectrum. This im-

Table 1. Ratio of the total SNR of P_0 , P_2 , and P_4 and the SNR of the real-space power spectrum with no photo- z errors and $n = 0.03 h^3 \text{Mpc}^{-3}$. This ratio is computed from 0.05 to $0.3 h \text{Mpc}^{-1}$, the range of scales used for BAO analyses in §6.

$n [h^3 \text{Mpc}^{-3}]$	$\sigma_z [\%]$	$r_{\text{SNR}} = \frac{\text{SNR}[\sigma_z]}{\text{SNR}_{r[\sigma_z=0]}}$
10^{-2}	0	1.00
10^{-2}	0.3	0.61
10^{-2}	0.5	0.52
10^{-2}	1.0	0.39
10^{-3}	0	0.70
10^{-3}	0.3	0.40
10^{-3}	0.5	0.31
10^{-3}	1.0	0.22
10^{-4}	0	0.21
10^{-4}	0.3	0.11
10^{-4}	0.5	0.08
10^{-4}	1.0	0.05

plies that, in the regime where shot noise is subdominant and despite the clustering enhancement due to large-scale RSD, in redshift space the SNR of power spectrum moments is lower than that in real space. This confirms the predictions of the toy model introduced in the previous section.

For samples with photo- z errors, we appreciate an increase in the SNR relative to the case with no photo- z errors on scales where $k \sigma_{\text{eff}} \simeq 1$, and a decrease on scales where the contribution of shot noise is the dominant in Eq. 16. Moreover, for $\sigma_z \lesssim 0.5\%$, the enhancement occurs on the scales where BAO are located. As BAO are suppressed by the non-linear evolution of the matter density field and RSD, this enhancement could imply that stronger cosmological constraints are derived from samples with sub-percent photo- z errors. We will return to this in the next section. Note that these apparent advantages may disappear after applying reconstruction procedures to the density field.

In Table 1 we show the ratio between the total SNR of P_0 , P_2 , and P_4 (computed taking into account the covariances among them, see Fig. 3) and that of the real-space power spectrum with no photo- z errors and $n = 0.03 h^3 \text{Mpc}^{-3}$. This ratio, r_{SNR} , is computed from 0.05 to $0.3 h \text{Mpc}^{-1}$, the range of scales that we use for BAO analyses in §6. We find that $r_{\text{SNR}} = 1$ for samples with no photo- z errors and $n = 10^{-2} h^3 \text{Mpc}^{-3}$, and thus there is the same amount of information in redshift space as in real space. Nevertheless, this information is not equally distributed in both spaces. In real space and for samples with no photo- z errors all the information is stored in the $\ell = 0$ moment, whereas in redshift space it is distributed between the $\ell = 0, 2$, and 4 moments. In this case, we find that the $\ell = 0$ moment accounts for $\simeq 97\%$ of the signal, the $\ell = 2$ moment the remaining $\simeq 3\%$, and the $\ell = 4$ moment does not contain any new information. Examining samples with a lower number density we find that the $\ell = 0$ moment encodes even more information, whereas P_4 starts to provide as much information as P_2 . This motivates the analysis of P_0 , P_2 , and P_4 in §6.

The results of Table 1 indicate that the value of r_{SNR} decreases by increasing the size of photo- z errors. This is somewhat expected, as we can see in Fig. 4 that the increment in the SNR for samples with photo- z errors only occurs on large scales, whereas on small scales the SNR is reduced.

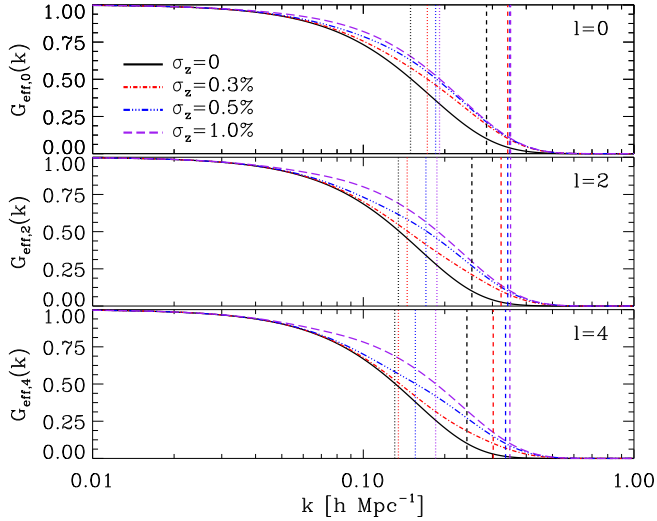


Figure 5. Suppression of BAO due to the combined effect of photo- z errors, non-linearities, and RSD. The top, middle, and bottom panels show the results for P_0 , P_2 , and P_4 , respectively. Dotted and dashed lines indicate when the suppression is greater than a factor of 2 and 10, respectively. The suppression of BAO is weaker for samples with photo- z errors because they decrease the weight of k -modes parallel to the LOS in the angular average, where in redshift space these modes are more suppressed than the perpendicular ones owing to RSD.

4 EFFECT OF PHOTOMETRIC REDSHIFT ERRORS ON BAO

In this section we investigate the effect of photo- z errors on the BAO feature imprinted in power spectrum moments. In §4.1 we study the suppression of BAO due to the combined effect of photo- z errors, the non-linear evolution of the matter density field, and RSD. In §4.2 we analyse the cosmological information encoded in BAO, in §4.3 we introduce a model to estimate the uncertainty in measuring the BAO scale, and in §4.4 we address how to extract cosmological information from the joint analysis of power spectrum moments.

4.1 The shape of the BAO signal

Let us begin by considering the following quantity:

$$B_\ell(k) \equiv \frac{P_\ell(k)}{P_\ell^{\text{sm}}(k)} - 1, \quad (21)$$

where P_ℓ^{sm} is a no-wiggle version of P_ℓ . This is a quantity with the same broadband shape as P_ℓ but no BAO. Therefore, B_ℓ is insensitive to the overall shape of the observed moments and isolates the BAO wiggles.

Motivated by Renormalized Perturbation Theory (Crocco & Scoccimarro 2008), we write the non-linear redshift-space power spectrum as:

$$P(k, \mu) = [P_{\text{lin}}(k) G(k, \mu) + P_{\text{mc}}(k, \mu)] b^2 \mathcal{F}^2, \quad (22)$$

where P_{lin} is the linear theory power spectrum in real space, P_{mc} denotes contribution of the coupling between different k -modes, and G is a propagator that controls the suppression of

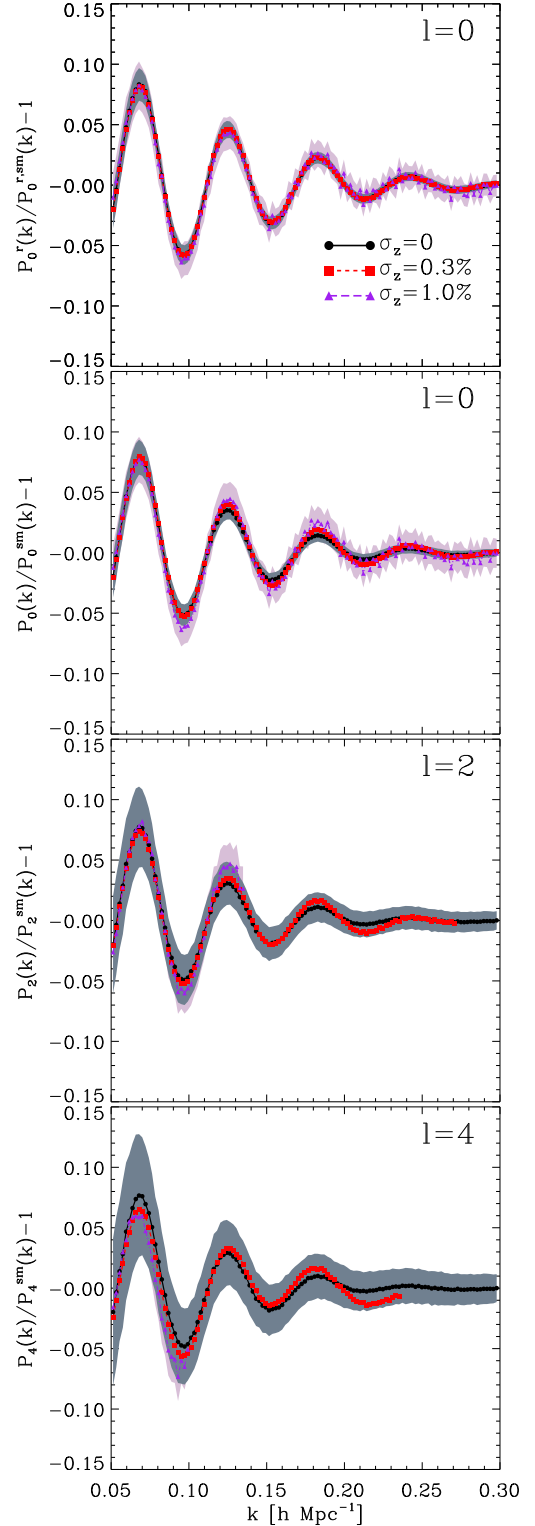


Figure 6. Average B_ℓ computed using 1000 samples from the COLA ensemble with $n = 0.01 h^3 \text{Mpc}^{-3}$ for P_0^r , P_0 , P_2 , and P_4 . The grey and purple areas denote the 1σ confidence region for samples with $\sigma_z = 0$ and 1%, respectively. For samples with photo- z errors we do not show the results up to $k \sim 0.3 h \text{Mpc}^{-1}$ because our procedure for extracting B_ℓ does not work well on scales where power spectrum moments are dominated by shot noise. In real space the amplitude of BAO is not modified by photo- z errors, whereas in redshift space it grows with their size. This confirms the predictions of Fig.5.

BAO due to non-linearities and RSD. This propagator is well approximated by a 2D exponential function:

$$G(k, \mu) = \exp \left\{ - \left[(1 - \mu^2) k^2 \sigma_{\perp}^2 + \mu^2 k^2 \sigma_{\parallel}^2 \right] \right\}, \quad (23)$$

where σ_{\parallel} and σ_{\perp} are parameters that control the suppression of k -modes along and perpendicular to the LOS, respectively. Note that, in redshift space $\sigma_{\parallel} > \sigma_{\perp}$. This is a consequence of peculiar velocities and the non-linear mapping between real and redshift-space positions, and it implies that the larger the value of μ , the greater the suppression of BAO for a given wavemode (e.g., Seo & Eisenstein 2007; Sánchez et al. 2008).

Let us now write a theoretical model for B_{ℓ} :

$$B_{\ell}(k) \simeq B_{\text{lin}}(k) G_{\text{eff},\ell}(k), \quad (24)$$

where $B_{\text{lin}} = P_{\text{lin}}/P_{\text{lin}}^{\text{sm}} - 1$, and

$$G_{\text{eff},\ell}(k) = \frac{\langle G(k, \mu) \mu^{\ell} \mathcal{F}^2 \rangle_{\mathbf{k}}}{\langle \mu^{\ell} \mathcal{F}^2 \rangle_{\mathbf{k}}}, \quad (25)$$

In deriving these expressions, we have assumed that $P \simeq [P_{\text{lin}}^{\text{sm}} + (P_{\text{lin}} - P_{\text{lin}}^{\text{sm}})G]b^2\mathcal{F}^2$ and $P^{\text{sm}} \simeq P_{\text{lin}}^{\text{sm}}b^2\mathcal{F}^2$. These assumptions are not strictly correct because they do not take into account the P_{mc} term in Eq. 22, and thus Eq. 25 does not predict a shift in the BAO scale due to non-linearities as the full model does (Crocco & Scoccimarro 2008).

The term $G_{\text{eff},\ell}$ gives the effective suppression of BAO in P_{ℓ} , as a function of the scale. As we can see, this quantity is a weighted average of $G(k, \mu)$, where the weights are given by photo- z errors and RSD. Therefore, a balance between these two aspects will determine the final appearance of BAO, as we will see next.

4.1.1 The Gaussian case and comparison with simulations

In the particular case of Gaussian photo- z errors, $G_{\text{eff},\ell}$ has an analytic expression. In the top, middle, and bottom panels of Fig. 5 we show $G_{\text{eff},0}$, $G_{\text{eff},2}$, and $G_{\text{eff},4}$, respectively. To build this figure we used $\sigma_{\parallel} = 6.8 h^{-1} \text{Mpc}$ and $\sigma_{\perp} = 4.3 h^{-1} \text{Mpc}$ (these values were set by our fits to the numerical simulations presented in §6). The vertical dotted and dashed lines indicate the scale at which the suppression of BAO is 50% and 90%, respectively.

As we can see, the BAO suppression is *weaker* for samples with larger photo- z errors. This has an interesting consequence, *photo- z errors make BAO wiggles to appear sharper*. Furthermore, for a given photo- z error, the suppression is stronger for higher order moments. This counter-intuitive result can be understood by recalling that LOS modes – where BAO smearing is more significant – contribute less to a given moment, thus, when photo- z are included, BAO appear more alike to the less-damped real-space case.

In order to check the accuracy of the predictions of Eq. 25, we measure B from the COLA ensemble. To obtain the no-wiggle power spectrum P_{ℓ}^{sm} , we fit P_{ℓ} using the following model

$$P_{\text{fit},\ell}(k) = A_{0,\ell} \langle \mu^{\ell} \mathcal{F}^2 \rangle_{\mathbf{k}} P_{\text{nw}}(k) + A_{1,\ell} k^2 + A_{2,\ell} k + A_{3,\ell} + A_{4,\ell} k^{-1} + A_{5,\ell} k^{-2} + A_{6,\ell} k^{-3}, \quad (26)$$

where P_{nw} is the non-wiggle power spectrum from

(Eisenstein & Hu 1998), and the factors $A_{i,\ell}$ give us enough freedom to fit the broadband shape of P_{ℓ} without fitting the oscillations. We explicitly show this in Fig. 6, where we display the average value of B measured from samples of the COLA ensemble with $n = 10^{-2} h^3 \text{Mpc}^{-3}$. In descending order, the panels show the results for P_0^r , P_0 , P_2 , and P_4 . Note that for samples with sub-percent photo- z errors, B_2 and B_4 are not displayed up to $k \sim 0.3 h \text{Mpc}^{-1}$. This is because on small scales the measurements start to be progressively dominated by shot noise.

We find that in real space the BAO feature is the identical in the cases with and without photo- z errors. This is expected from Eq. 25, as in real space $\sigma_{\parallel} = \sigma_{\perp}$, and thus $G_{\text{eff},0} = e^{-(k\sigma_{\perp})^2}$. However, in redshift space, BAO are less suppressed for samples with greater photo- z errors, confirming the predictions of Fig. 5 and our analytic model.

4.2 Cosmological information encoded in BAO

We now explore the cosmological information encoded in the BAO feature. Let us consider a given scale $k = \sqrt{k_{\parallel}^2 + k_{\perp}^2}$ and angle $\mu = k_{\parallel}/k$ in the two-dimensional power spectrum. Assuming a fiducial cosmology, they are observed as

$$k^{\text{fid}} = k/\alpha \equiv k\sqrt{\mu^2\alpha_{\parallel}^{-2} + (1 - \mu^2)\alpha_{\perp}^{-2}}, \quad (27)$$

$$\mu^{\text{fid}} = \epsilon\mu \equiv \frac{\mu}{\sqrt{\mu^2 + (1 - \mu^2)(\alpha_{\parallel}/\alpha_{\perp})^2}}, \quad (28)$$

where $\alpha_{\parallel} \equiv \frac{H^{\text{fid}}(z)r_s^{\text{fid}}}{H(z)r_s}$ and $\alpha_{\perp} \equiv \frac{D_A(z)r_s^{\text{fid}}}{D_A^{\text{fid}}(z)r_s}$. In the above expressions, r_s is the sound horizon scale, D_A is the angular diameter distance, H is the Hubble parameter, and fid denotes these quantities in the fiducial cosmology. The observed redshift-space power spectrum moments are thus

$$P_{\ell}(k/\alpha_{\ell}) = \alpha_{\parallel}^{-1} \alpha_{\perp}^{-2} \left\langle \epsilon^{\ell+1} \mu^{\ell} \left[1 + \epsilon^2 \mu^2 (\alpha_{\parallel}^2 \alpha_{\perp}^{-2} - 1) \right] \mathcal{F}^2(k/\alpha, \epsilon\mu) P_0^r(k/\alpha) \right\rangle_{\mathbf{k}}, \quad (29)$$

where assuming an incorrect cosmology would cause isotropic and anisotropic deformations. For the full expression of deformations in observed multipoles see Padmanabhan & White (2008) in Fourier space and Xu et al. (2013) in configuration space.

Since here we are mostly interested in the information encoded in the BAO scale, we follow Ross et al. (2015, R15 hereafter) and focus only on the stretch parameters α_{ℓ} as a function of α_{\parallel} and α_{\perp} ¹. As in R15, we will also assume that the information on α_{ℓ} is separable from the overall shape of power spectrum moments and that the information in different μ bins is independent. Under these assumptions:

$$\alpha_{\ell}(k) = \frac{\langle \mu^{\ell} \mathcal{F}^2 \alpha \rangle_{\mathbf{k}}}{\langle \mu^{\ell} \mathcal{F}^2 \rangle_{\mathbf{k}}}, \quad (30)$$

where the scale-dependence of α_{ℓ} emerges from the scale-dependence of \mathcal{F}^2 . The previous expression reduces to Eq. 6 of

¹ In what follows we will assume that $\alpha_{\parallel}^2/\alpha_{\perp}^2 = 1$ and thus $\epsilon = 1$.

R15 for samples with no photo- z errors nor small-scale RSD. Therefore, small-scale RSD and/or photo- z errors induce a scale-dependence in the stretch parameter.

As in R15, we find that the first order expansion of α_ℓ around the fiducial solution can be expressed as $\alpha_\ell(k) = \alpha_\parallel^{m_\ell(k)} \alpha_\perp^{n_\ell(k)}$, where m_ℓ and n_ℓ are given by:

$$m_\ell(k) \equiv \left. \frac{\partial \langle \alpha_\ell \rangle}{\partial \alpha_\parallel} \right|_{\alpha_\parallel = \alpha_\perp = 1} = \frac{\langle \mu^{\ell+2} \mathcal{F}^2 \rangle_{\mathbf{k}}}{\langle \mu^\ell \mathcal{F}^2 \rangle_{\mathbf{k}}}, \quad (31)$$

$$n_\ell(k) \equiv \left. \frac{\partial \langle \alpha_\ell \rangle}{\partial \alpha_\perp} \right|_{\alpha_\parallel = \alpha_\perp = 1} = 1 - m_\ell(k), \quad (32)$$

where the higher the value of m_ℓ , the more sensitive α_ℓ is to the Hubble parameter. For the case of Gaussian photo- z errors, m_ℓ and n_ℓ have analytic expressions.

Going back to the stretch parameter, the known case with $m_0 = 1/3$ and $n_0 = 2/3$ (Eisenstein et al. 2005) is only recovered in real space without photo- z errors. In redshift space, there is a dependence of m_ℓ and n_ℓ on β even if $\sigma_z = 0$. In general, the effect of photo- z errors and small-scale RSD is to decrease the sensitivity of α_ℓ on H , whereas large-scale RSD have the opposite effect. Nonetheless, the exact degeneracy between α_\parallel and α_\perp also depends on the properties of analysed sample, such as its large-scale bias.

4.3 Toy model for the uncertainty in the stretch parameter

In §3.3 we studied the SNR of power spectrum moments and in the previous section we showed that the suppression of the BAO feature depends on $G_{\text{eff},\ell}$. In this section we use this to derive an analytic estimation of the uncertainty in α_ℓ as a function of large-scale bias, number density, photo- z error, and cosmology.

To build an estimator for the precision measuring α_ℓ , we will assume that its uncertainty is given by the convolution of the one measuring P_ℓ and the amplitude of BAO wiggles in P_ℓ . The latter obviously depends on the suppression of BAO due to non-linearities and RSD, which as we explained before is captured by $G_{\text{eff},\ell}$. For conventional approaches using Fisher matrix forecast see for instance Seo & Eisenstein (2003).

We estimate the amplitude of unsuppressed BAO in linear theory by measuring the absolute value of the local extrema of $1 + B_{\text{lin}}$. Then, we do a linear fit of these values, B_{amp} . The product of this quantity and Eq. 25, $G_{\text{eff},\ell} B_{\text{amp}}$, gives thus the maximum amplitude of BAO wiggles in P_ℓ under the presence of non-linearities, RSD, and photo- z errors.

In BAO analyses, the stretch parameter α_ℓ is extracted from an interval of scales. As this parameter is scale-dependent due to small-scale velocities and photo- z errors, it is useful to define an effective stretch parameter $\alpha_{\text{eff},\ell}$. We estimate the uncertainty in this parameter as the uncertainty in a moment times the amplitude of BAO wiggles

$$\hat{\sigma}[\alpha_{\text{eff},\ell}] = \frac{A_\ell}{(k_{\text{max}} - k_{\text{min}})^c} \left(\int_{k_{\text{min}}}^{k_{\text{max}}} dk \frac{P_\ell^2 G_{\text{eff},\ell}^2 B_{\text{amp}}^2}{\sigma^2[P_\ell]} \right)^{-0.5}, \quad (33)$$

where A_ℓ and c are free parameters. Note that we assumed that the off-diagonal terms of the covariance matrices of power spectrum moments are negligible on the range of scales where BAO are located (see §3.2.3).

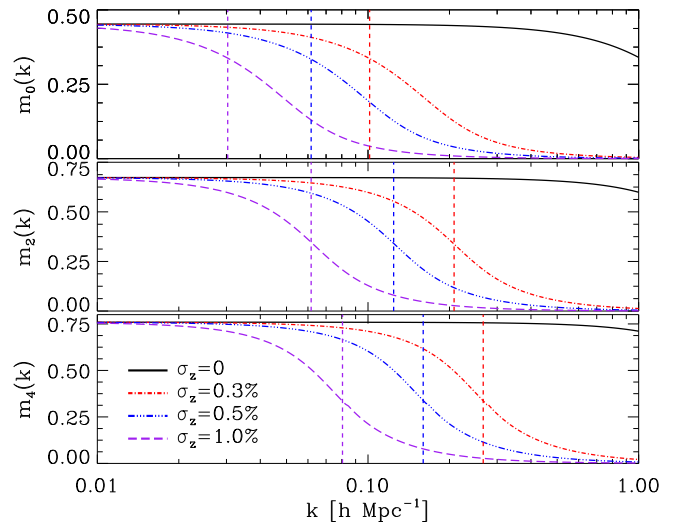


Figure 7. Sensitivity of BAO to the Hubble parameter as function of the scale, m_ℓ . The top, medium, and bottom panels show the results for BAO in P_0 , P_2 , and P_4 , respectively. The vertical lines indicate the scale at which the dependence of BAO on the Hubble parameter is smaller than for samples with no photo- z errors in real space ($m = 1/3$). As expected, the larger the photo- z error, the smaller is the dependence of BAO on the Hubble parameter. We can see that samples with no photo- z errors also present a dependence of m_ℓ on the scale, which occurs due to small-scale velocities.

4.4 The scale-dependence of cosmological information

In §4.2 we showed that there is a scale dependence for the cosmological information encoded in BAO, which introduces an additional complication while extracting information from BAO analyses. We present in the top, middle, and bottom panel of Fig. 7 the value of m_0 , m_2 , and m_4 as a function of the scale, respectively. Solid lines indicate the results for different photo- z errors, $b = 1$, and our adopted cosmology (c.f. §2.1). Dashed lines denote when the sensitivity of BAO to the Hubble parameter is the same as in real-space, $m = 1/3$. As we can see, the higher is the order of the moment, the greater is the sensitivity on the Hubble parameter. For example, if we look at samples with $\sigma_z = 0.3\%$, m_0 , m_2 , and m_4 are greater than $1/3$ up to $k \simeq 0.1$, 0.2 , and $0.3 h \text{Mpc}^{-1}$, respectively. Therefore, the analysis of BAO in the $\ell = 4$ moment of samples with $\sigma_z = 0.3\%$ is more sensitive to the Hubble parameter than in real space. This highlights the importance of not only analysing BAO in the $l = 0$ and $l = 2$ moments. In addition, we can see that there is a scale dependence of m_ℓ for samples with no photo- z errors, which is caused by small-scale velocities.

We can derive the relation between the precision in measuring α_ℓ and the radial and perpendicular components of α – Hubble parameter and angular diameter distance, respectively – using Eqs. 31 and 32:

$$\sigma^2[\alpha_{\ell,\ell'}] = m_\ell^2 \sigma^2[\alpha_\parallel] + n_{\ell'}^2 \sigma^2[\alpha_\perp], \quad (34)$$

where the uncertainty in the radial and perpendicular components are $\sigma[\alpha_\parallel]$ and $\sigma[\alpha_\perp]$, respectively. Consequently, to extract the precision in measuring both components we need to perform a joint fit of at least two power spectrum moments.

In the same way that we computed an effective value for

the stretch parameter in the previous section, we can now estimate an overall degeneracy between the parallel and perpendicular components of α_ℓ when they are estimated from an interval of scales, $m_{\text{eff},\ell}$. To do this, we compute the variance-weighted average of m_ℓ and n_ℓ over the desired k -interval, where the variances are given by Eq. 33. Explicitly,

$$m_{\text{eff},\ell} = \frac{\int_{k_{\text{min}}}^{k_{\text{max}}} dk \frac{m_\ell P_\ell^2 G_{\text{eff},\ell}^2 B_{\text{amp}}^2}{\sigma^2[P_\ell]}}{\int_{k_{\text{min}}}^{k_{\text{max}}} dk \frac{P_\ell^2 G_{\text{eff},\ell}^2 B_{\text{amp}}^2}{\sigma^2[P_\ell]}}, \quad (35)$$

$$n_{\text{eff},\ell} = 1 - m_{\text{eff},\ell}, \quad (36)$$

and thus, the degeneracy between the overall precision in the parallel and perpendicular components of $\alpha_{\text{eff},\ell}$ is given by

$$\sigma^2[\alpha_{\text{eff},\ell}] = m_{\text{eff},\ell}^2 \sigma^2[\alpha_{\parallel}] + n_{\text{eff},\ell}^2 \sigma^2[\alpha_{\perp}]. \quad (37)$$

Nevertheless, we are interested in the precision measuring H and D_A . In §6 we conduct a joint analysis of BAO in P_0 , P_2 , and P_4 to compute their uncertainties, as it is required the analysis of at least two moments to break the degeneracy in cosmological information along and perpendicular to the LOS. From now on, we drop the subindex eff for simplicity. In this way,

$$\Sigma = \mathbf{M}^+ \mathbf{E} (\mathbf{M}^+)^T, \quad (38)$$

$$\Sigma = \begin{pmatrix} \sigma^2[\alpha_{\parallel}] & \sigma[\alpha_{\parallel,\perp}] \\ \sigma[\alpha_{\parallel,\perp}] & \sigma^2[\alpha_{\perp}] \end{pmatrix}, \quad (39)$$

$$\mathbf{M} = \begin{pmatrix} m_0 & n_0 \\ m_2 & n_2 \\ m_4 & n_4 \end{pmatrix}, \quad (40)$$

$$\mathbf{E} = \begin{pmatrix} \sigma^2[\alpha_0] & \sigma[\alpha_{0,2}] & \sigma[\alpha_{0,4}] \\ \sigma[\alpha_{0,2}] & \sigma^2[\alpha_2] & \sigma[\alpha_{2,4}] \\ \sigma[\alpha_{0,4}] & \sigma[\alpha_{2,4}] & \sigma^2[\alpha_4] \end{pmatrix}, \quad (41)$$

where \mathbf{M}^+ is the pseudoinverse of \mathbf{M} (Moore 1920; Bjerhammar 1951; Penrose 1955), Σ is the covariance matrix of H and D_A , and \mathbf{E} is computed from BAO analysis of power spectrum moments.

5 EXTRACTING INFORMATION FROM BAO

In the previous sections we showed how photo- z errors modify the amplitude of power spectrum moments, their variances, the suppression of BAO, and the cosmological information encoded in them. In this section we employ all this information to create a model to unbiasedly extract the BAO scale, α , from observational and/or simulated data, even under the presence of photo- z errors. We will employ this model on simulated catalogues in §6.

5.1 Modelling power spectrum moments

Based on the expressions provided in §4.1, we can write the following four parameter model for power spectrum moments:

$$P_{T,\ell} = P_\ell^{\text{sm}}(k) [B_{\text{lin}}(k/\alpha_\ell) G_\ell(k/\alpha_\ell, \sigma_{\text{eff}}, \sigma_\perp, f) + 1] \quad (42)$$

where P_ℓ^{sm} is computed using the same approach as in §4.1, the parameter α_ℓ allows for stretching of the BAO, σ_\perp and $f = \sigma_{\parallel}/\sigma_\perp$ control BAO suppression. Photo- z errors enter

only through G_ℓ . Note that all these parameters only appear in the expression for B_{lin} and G_ℓ , and thus they are only constrained by BAO information, i.e. our model extracts cosmological information regardless of the overall shape of the analysed moment.

In the following sections we will fix σ_{eff} to the correct value. We do this to break a degeneracy between σ_\perp and σ_{eff} , as both control the suppression of BAO. In any case, we checked that if include both parameters are let them vary, we recover the same results for α_ℓ .

5.2 Parameter Likelihood Calculation

To extract the information encoded in BAO, we jointly fit P_0 , P_2 , and P_4 . For this, we assume that the probability of observing $\mathbf{d} = [P_0, P_2, P_4]$ is given by a multivariate Gaussian distribution:

$$\Pr(\mathbf{d}|\pi) \propto \exp \left[-\frac{1}{2} (\mathbf{d} - \mathbf{t})^T \mathbf{C}^{-1} (\mathbf{d} - \mathbf{t}) \right], \quad (43)$$

where $\mathbf{t}(k, \pi) = [P_{T,0}, P_{T,2}, P_{T,4}]$, and $\pi = \{\alpha_0, \alpha_2, \alpha_4, \sigma_\perp, f\}$ denote the five free parameters of our model. The priors on these parameters are assumed to be flat over the range: $\alpha_\ell \in [0.75, 1.25]$ and $\sigma_\perp \in [0.5, 10]$, and $f \in [1, 10]$. We set the minimum value of f to be 1 because in redshift space the combination of RSD and non-linearities make k -modes along the LOS to be the most suppressed (see §4.1). We note that the results do not change if we set wider priors. \mathbf{C}^{-1} is the data precision matrix of \mathbf{d} , which we compute from the COLA ensemble as described in §2.2. The interval of scales considered is $k = [0.05 - 0.30] h \text{ Mpc}^{-1}$.

We sample the posterior probability distribution function of π employing the publicly available code `emcee` (Foreman-Mackey et al. 2013). This code is an affine invariant MCMC ensemble sampler that has been widely tested and used in multiple scientific studies. We configure the code to analyse \mathbf{d} using a chain of 100 random walkers with 5000 steps each, and a burn-in phase of 500 steps. We checked that this burn-in phase is sufficient to obtain well-behaved chains.

Additionally, we checked that the standard deviations of the best-fit values from the COLA ensemble are compatible with the uncertainties estimated from the likelihood of each simulated catalogue.

6 RESULTS FROM SIMULATED CATALOGUES

In this section we start by studying the quality of the BAO fitting model introduced in the previous section. Then, we apply this model to simulated catalogues with different photo- z errors and number densities. In addition, we study whether introducing photo- z errors following PDFs different from Gaussian impacts our results. Finally, we present a simple procedure to undo the effect of peculiar velocities on power spectrum moments.

We note that in this section we analyse power spectrum moments computed from DM particles. In principle, this could introduce a shift in the stretch parameter with respect to computing power spectrum moments from haloes/galaxies. However, Angulo et al. (2014) addressed this by measuring the stretch parameter from the real- and redshift-space monopole of galaxies selected by star formation and stellar mass in the Millennium XXL simulation (Angulo et al. 2012), finding no

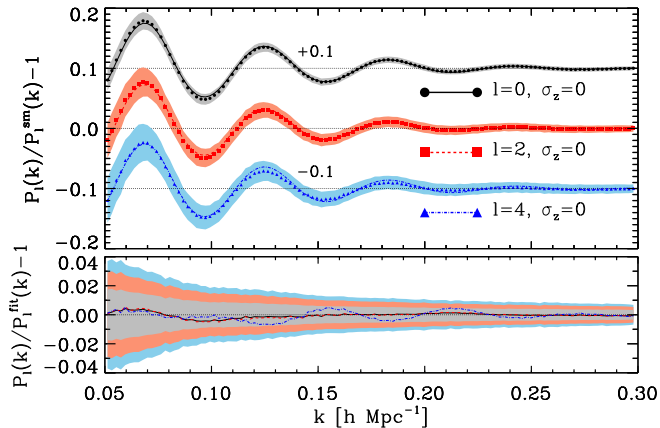


Figure 8. Relative difference between P_0 , P_2 , P_4 and their no-wiggle versions for samples with no photo- z errors and $n = 10^{-2} h^3 \text{Mpc}^{-3}$. Symbols and lines display the average results from the COLA ensemble and the average best-fit to each mock using Eq. 42, respectively. Coloured regions indicate the 1σ region of the scatter from mock-to-mock. The bottom panel shows the relative difference between the average data and model. The precision of our template is to within 1%, which is greater than the typical scatter from mock-to-mock.

additional shifts with respect the stretch parameter measured from DM particles. Therefore, we will restrict our analysis to DM particles.

6.1 Quality of our model

In Fig. 8 we show the result of fitting the model introduced in Eq. 42 to samples from the COLA ensemble with $\sigma_z = 0$ and $n = 10^{-2} h^3 \text{Mpc}^{-3}$. Symbols indicate the average value of B_ℓ computed from the COLA ensemble, and lines the average of the best-fit to each mock. We display the results for $\ell = 0$, $\ell = 2$, and $\ell = 4$ in black, red, and blue, respectively, where they are offset for clarity. Shaded areas enclose the 1σ region from mock-to-mock. In the bottom panel we plot the relative difference between the model and data, where we can see that in all cases the typical deviations are statistically insignificant. In addition, our model reproduces the simulated data to within 1% on the scales shown, which is more than enough for the next generation of galaxy surveys. We also checked that we obtain similar results for samples with sub-percent photo- z errors.

6.2 Effect of redshift errors

In this section we apply our BAO analysis procedure to power spectrum moments of samples with $n = 10^{-2} h^3 \text{Mpc}^{-3}$ and Gaussian photo- z errors of different sizes.

We start by studying the shift in the stretch parameter with respect to its fiducial value, $\alpha_\ell - 1$, from the BAO analysis of real- and redshift-space power spectrum moments of 1000 samples from the COLA ensemble. In the left and right panels of Fig. 9 we present the distribution of these parameters and their uncertainties, respectively, from the analysis of samples with different photo- z errors. Arrows point to the mean of each distribution, and we gather these values in Table 2. As we can see in the left panels, the average value of $\alpha_\ell - 1$ is compatible with zero at the 1σ level for all samples. This implies that

Table 2. Average results extracted from the MCMC analysis of 1000 independent catalogues of DM particles with $n = 10^{-2} h^3 \text{Mpc}^{-3}$. We show the average value of α_ℓ , $\bar{\alpha}_\ell$, and the average uncertainty measuring this parameter after marginalising over the other free parameters in the model.

	$\bar{\alpha}_0 - 1$ (%)	$\bar{\alpha}_2 - 1$ (%)	$\bar{\alpha}_4 - 1$ (%)
Real space			
0	0.20 ± 0.22	0.23 ± 0.40	0.24 ± 0.52
0.3	0.19 ± 0.25	0.20 ± 0.50	0.44 ± 0.78
0.5	0.14 ± 0.30	0.20 ± 0.78	0.11 ± 1.47
1.0	0.30 ± 0.40	0.29 ± 1.62	2.10 ± 4.81
Redshift space			
0	0.32 ± 0.34	0.40 ± 0.68	0.44 ± 0.93
0.3	0.28 ± 0.28	0.34 ± 0.62	0.33 ± 0.93
0.5	0.09 ± 0.31	0.23 ± 0.79	0.18 ± 1.20
1.0	0.09 ± 0.42	0.38 ± 1.92	-1.73 ± 3.62

for samples with sub-percent photo- z errors our estimator is unbiased relative to the case with no errors. However, for larger photo- z errors this is no longer correct, as we can see for α_4 and $\sigma_z = 1.0\%$. This is because our procedure to calculate a smooth version of power spectrum moments does not work well if the amplitude of the moment is of the order of the shot noise level.

In real and redshift space the stretch parameter presents a small and positive shift, which is caused by the non-linear evolution of the matter density field (e.g., Angulo et al. 2008; Crocce & Scoccimarro 2008; Smith et al. 2008; Padmanabhan & White 2009). We also find that this shift slightly decreases with the size of photo- z errors. This is because photo- z errors strongly suppress k -modes along the LOS on small scales, which are the k -modes that present a greater coupling due to non-linearities and RSD, and thus reduce the effective shift in the volume-averaged stretch parameters. Whereas the shifts that we find are statistically significant for the volume of the COLA ensemble, $27000 h^{-3} \text{Gpc}^3$, for a single simulation they are compatible with zero to within 1σ . Furthermore, these shifts can in principle be approximately corrected for via reconstruction algorithms² (e.g., Eisenstein et al. 2007; Schmittfull et al. 2015) or by recalibrating the estimator employed.

The top-right panel of Fig. 9 displays the uncertainty in the stretch parameter measured from samples in real space. As we expect, the precision measuring α_ℓ^r decreases with the size of photo- z errors. This is the consequence of photo- z errors suppressing the clustering on small scales, which increases the relative contribution of shot noise to the variance, and thus reduces the SNR.

In redshift space the precision measuring α_ℓ is a combination of the effect explained in the previous paragraph and the fact that photo- z errors reduce the overall suppression of BAO (see Fig. 5). As explained in §4.1, they reduce the weight of k -modes parallel to the LOS when doing the angular average of the 3D power spectrum, where these modes are noisier than the perpendicular ones owing to RSD. In the bottom-right panel we can see that the balance between both effects causes

² We note that this procedure has never been applied to reconstruct the 3D density field of galaxy samples with photo- z errors.

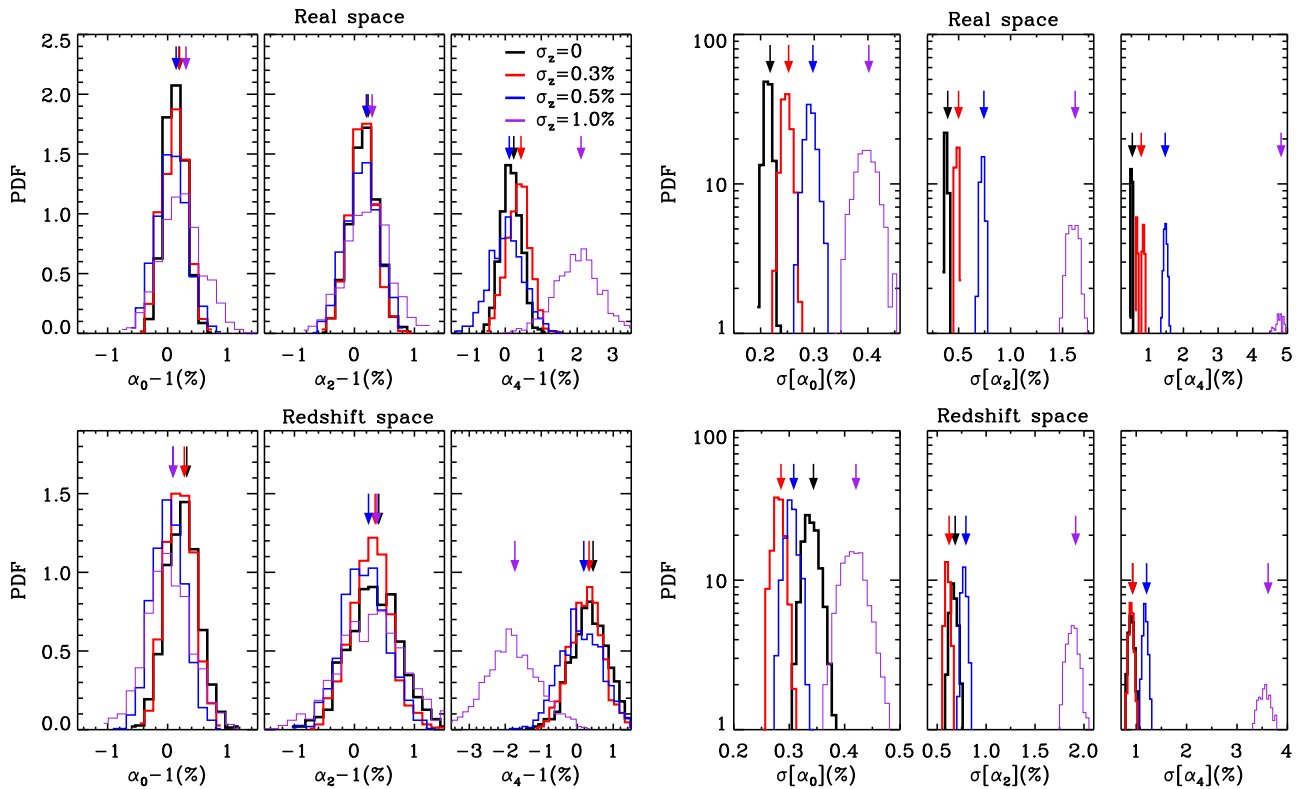


Figure 9. Distribution of α_ℓ (left panels) and their uncertainties (right panels) from MCMC analysis of 1000 independent catalogues of DM particles with $n = 10^{-2} h^3 \text{Mpc}^{-3}$ and different Gaussian photo- z errors. The precision measuring α_ℓ is computed after marginalising over the other parameters in the model. The top and bottom rows show the results in real and redshift space, respectively. Arrows point to the mean of each distribution. For samples with sub-percent photo- z errors, the value of α_ℓ is compatible with the fiducial cosmology at the 1σ level ($\alpha_\ell - 1 = 0$). Therefore, sub-percent photo- z errors do not introduce an additional shift in the position of BAO. As we can see in the right panels, in real space the precision measuring α_ℓ decreases with the size of photo- z errors. Nevertheless, in redshift space samples with small photo- z errors measure α_0 with more precision than samples with no errors. This is because the suppression of BAO in power spectrum moments decreases with the size of photo- z errors (see §4.1).

$\sigma[\alpha_\ell]$ not to be a monotonic function of the size of photo- z errors. We find that α_0 can be measured with more precision from samples with small photo- z errors ($\sigma_z \leq 0.5\%$) than from samples with no errors. Nevertheless, if we increase the size of photo- z errors this is no longer true, for instance $\sigma[\alpha_0]$ for samples with $\sigma_z = 1.0\%$ is greater than for samples with no photo- z errors. For higher order moments the results are different because the range of scales for which the variance is not dominated by shot noise is smaller. However, for samples with $\sigma_z = 0.3\%$ we still find that α_2 and α_4 can be measured with more precision or the same precision, respectively, as from samples with no photo- z errors.

A by-product of the MCMC analysis of power spectrum moments is the value of the parameters (σ_\perp, f) , which encode the suppression of the moments perpendicular and parallel to the LOS ($\sigma_\parallel = f\sigma_\perp$), respectively. We find that their average value and uncertainty are approximately the same independently of the size of photo- z errors. For samples with no photo- z errors they are $\sigma_\perp = 4.02 \pm 0.13$ and $f = 1.06 \pm 0.05$ in real space, and $\sigma_\perp = 4.29 \pm 0.38$ and $f = 1.68 \pm 0.25$ in redshift space. As expected, RSD increase the suppression of k -modes parallel to the LOS: for the COLA ensemble at $z = 1$ this suppression is 68% greater than for k -modes perpendicular to the LOS. This is the main reason behind getting more

precise results in α_ℓ from samples in redshift space with sub-percent photo- z errors for which shot noise is not relevant on BAO scales.

6.3 Effect of different PDFs for photometric redshift errors

In general, photo- z errors do not follow a Gaussian PDF. For instance, the comparison between photometric and spectroscopic redshifts in the COSMOS survey shows that the PDF of photo- z errors is well described by a Lorentzian variate (Ilbert et al. 2009). Additionally, for low redshift galaxies the PDF of photo- z errors usually shows a tail towards higher redshifts, which is a natural consequence of imposing $z > 0$ in an otherwise symmetric PDF. In this section we investigate whether photo- z drawn from non-Gaussian PDFs may bias the results from BAO analyses when assuming that they are drawn from a Gaussian PDF.

We will consider two families of functional forms for photo- z errors:

i) PDF1:

$$\text{Pr}[\delta r_z] dz = \frac{1}{2\Delta\Gamma\left(1 + \frac{1}{p_1}\right)} \exp\left(-\left|\frac{z}{\Delta}\right|^{p_1}\right) dz, \quad (44)$$

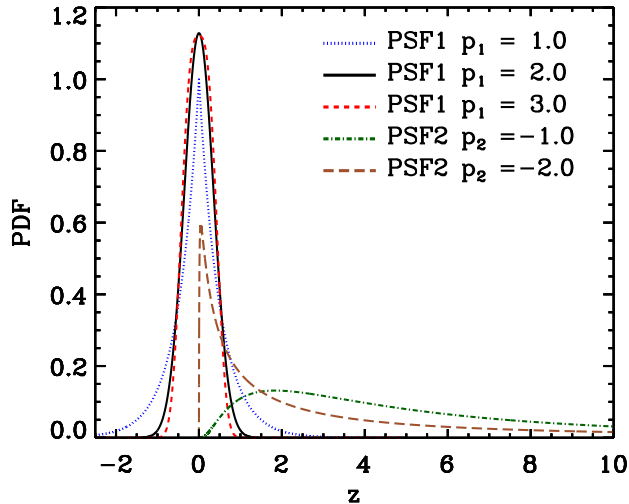


Figure 10. Distributions from which photo- z errors are drawn in §6.3. The parameter p_1 controls the excess kurtosis of distributions from PDF1 and p_2 the skewness and excess kurtosis of that from PDF2. All distributions from PDF1 are symmetric (zero skewness), where the ones with $p_1 = 2$, $p_1 > 2$, and $p_1 < 2$ are Gaussians, boxier than Gaussians, and Gaussians with extended wings like Lorentzians, respectively. The distributions from PDF2 are positively skewed, and their skewness and excess kurtosis grow with p_2 .

ii) PDF2:

$$\Pr[\delta r_z] dz = \frac{-1}{p_2 z \sqrt{2\pi}} \exp\left[-\frac{1}{2p_2^2} \ln^2\left(-\frac{p_2 z}{\Delta}\right)\right] dz, \quad (45)$$

where Γ is the Gamma function, Δ controls the width of the distributions, p_1 the excess kurtosis for the family PDF1, and p_2 the skewness and excess kurtosis for the family PDF2. The distributions from PDF1 are symmetric (zero skewness) and show different levels of excess kurtosis. We find that for $p_1 = 2$ the distributions of this family are Gaussians, for $p_1 < 2$ show extended wings like a Lorentzian, and for $p_1 > 2$ are boxier than a Gaussian. The distributions from PDF2 are asymmetric and not centred in zero. We find one famous distribution of this family for $\Delta = p_2$ and $p_2 < 0$, the log-normal distribution.

In Fig. 10 we display the PDF of distributions that we use to introduce photo- z errors in the COLA ensemble. We note that the ones with $p_2 \neq 0$ are in general more extreme than the PDF of photo- z errors from real data. Therefore, if we were to find that the results from BAO analyses assuming a Gaussian distribution are the same for all these distributions, we could conclude that BAO analyses are insensitive to the shape of the PDF of photo- z errors.

In Fig. 11 we present the value of α_0 , α_2 , and α_4 extracted from the BAO analysis of the average moments of 100 samples from the COLA ensemble after assuming a Gaussian PDF in the analysis. The number density of these samples is $n = 10^{-2} h^3 \text{Mpc}^{-3}$, their photo- z errors are drawn from the distributions displayed in Fig. 10, and the difference between the 84th and 16th percentiles of those distributions is set to be $\sigma_z = 0.3\%$. The grey coloured regions indicate the 1σ confidence region for a Gaussian PDF, and the error bars for the other distributions. For extreme PDFs, this could in principle introduce systematic errors in the estimation of α_ℓ . In practice we can see that even considering extreme PDFs and assuming a Gaussian PDF in the BAO analysis, the results are compati-

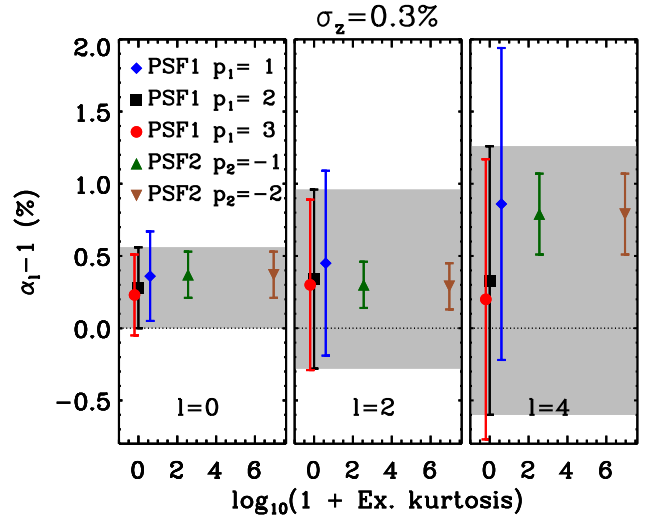


Figure 11. Shift and uncertainty in α_0 , α_2 , and α_4 from BAO analysis of 100 samples from the COLA ensemble with $n = 10^{-2} h^3 \text{Mpc}^{-3}$ and photo- z errors drawn from different PDFs, where in the analysis we assume that they are drawn from a Gaussian PDF. The grey coloured areas enclose the 1σ confidence region from the analysis of samples with Gaussian photo- z errors. The employed PDFs are shown in Fig. 10. Even for photo- z errors drawn from PDFs with large excess kurtosis and skewness, the results are compatible with the Gaussian case at the 1σ level.

ble to within 1σ . In addition, the shift in the stretch parameter is largely insensitive to the actual shape of the PDF.

In this section we have disregarded the possibility of interlopers - objects systematically assigned to incorrect redshifts. This may happen to unobscured quasars and star-forming galaxies in medium- and narrow-band surveys, as pairs of emission lines at different redshifts may fall in the same filters, which is translated into a redshift PDF with two or more peaks (see, e.g., fig. 4 of Chaves-Montero et al. 2017). If the percentage of interlopers is very small, at first order their net effect is to increase the shot noise level as they are uncorrelated with the main sample. They can be accounted for by artificially increasing the shot noise level. Nonetheless, if their amount is significant with respect to the main sample, they introduce anisotropies in the galaxy clustering (Lidz & Taylor 2016), where these anisotropies open the possibility of using AP-type tests (Alcock & Paczynski 1979) to correct for them.

We note that all expressions in this work are given for arbitrary PDFs. Therefore, if it is possible know the PDF of photo- z errors, its actual shape can be used in BAO analyses.

6.4 Extracting cosmological information from BAO and impact of number density

As explained in §6.2, the constraining power of BAO depends on the scale at which the shot noise level starts dominating the amplitude of power spectrum moments. In this section we address how the precision in measuring cosmological parameters from BAO analyses (H and D_A) depends on the number density of the analysed sample. For this, we re-analyse our COLA samples randomly diluted to have $\bar{n} = [10^{-2}, 3 \times 10^{-3}, 10^{-3}, 3 \times 10^{-4}, 10^{-4}] h^3 \text{Mpc}^{-3}$.

In the top and bottom panels of Fig. 12 we present the average precision in measuring σ_\perp and σ_\parallel from 1000 COLA

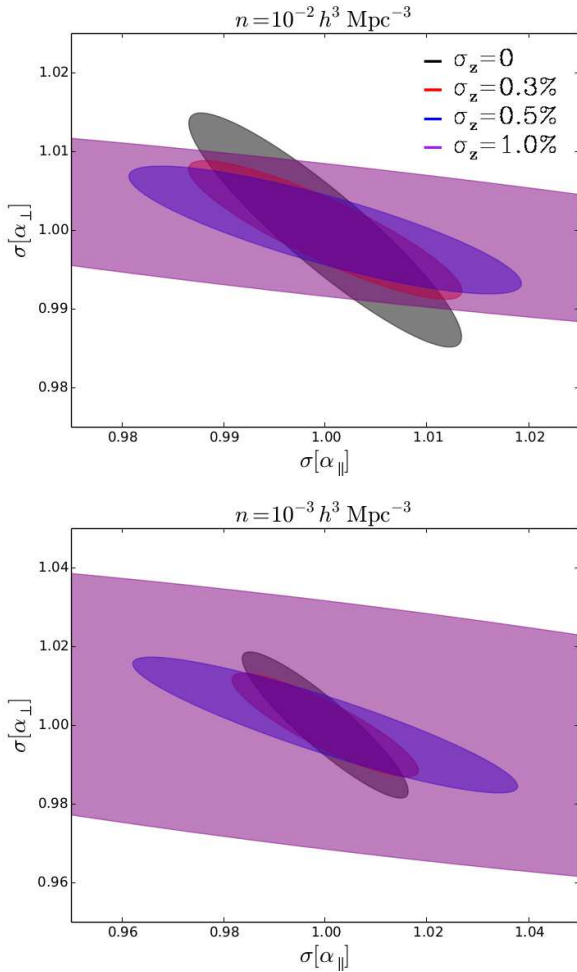


Figure 12. Uncertainty in the parallel and perpendicular components of the stretch parameter for samples with $n = 10^{-2}$ and $10^{-3} h^3 \text{Mpc}^{-3}$ (top and bottom panel, respectively), where they control the precision measuring H and D_A , respectively. As we can see, the uncertainty in H after marginalising over D_A grows with the size of photo- z errors, as the error ellipses rotate in the anti-clockwise direction. However, the FoM (inverse of the ellipse’s area) does not monotonically decrease with σ_z , which means that the combination of H and D_A is not always measured with more precision by samples with no photo- z errors from the analysis of power spectrum moments.

samples with $n = 10^{-2}$ and $10^{-3} h^3 \text{Mpc}^{-3}$, respectively. Contours enclose the 1σ confidence region for samples with different Gaussian photo- z errors, as stated in the legend. The uncertainty in σ_{\parallel} (after marginalising over σ_{\perp}) always increases with the size of photo- z errors, which is because the error ellipses rotate anticlockwise as photo- z errors grow. Nevertheless, the uncertainty in σ_{\perp} and the Figure-of-Merit (FoM) of this combination of parameters (the inverse of the ellipse’s area) do not monotonically grow with the size of photo- z errors. For the number densities studied here, we find that for $\sigma_z = 0.3\%$ the precision in measuring D_A is greater than for samples with $\sigma_z = 0$, which highlights that the analysis of power spectrum moments might not optimally extract the cosmological information encoded in BAO perpendicular to the LOS. We further explore this in the next section.

To continue exploring the constraints on cosmological parameters as a function of number density and photo- z errors,

in the left, middle, and right panels of Fig. 13 we display the precision in H , D_A , and the FoM of both parameters, respectively. The uncertainty in each parameter is computed after marginalising over the other. Symbols and lines indicate the results from simulations and the analytic model introduced in Eq. 33, respectively, where the free parameters of the model are fitted to reproduce the results from simulations. Their value is $A_0 = 0.35$, $A_2 = 0.50$, $A_4 = 0.55$, and $c = 0.3$. As expected, the uncertainty in H grows with the size of photo- z errors and by decreasing the number density. However, it is important to notice that the precision in H is the same for samples with $\sigma_z = 0.5\%$ and $n = 10^{-3} h^3 \text{Mpc}^{-3}$ and as for samples no photo- z errors and $10^{-4} h^3 \text{Mpc}^{-3}$. As spectro-photometric surveys detect in general fainter objects than spectroscopic surveys, future wide-field surveys with dozens of photometric bands such as J-PAS will be competitive with spectroscopic surveys measuring cosmological parameters from BAO analyses.

The precision measuring D_A and the FoM of H and D_A shows a non-monotonic behaviour with σ_z for samples with large number densities, whereas at smaller number densities they are proportional to the size of photo- z errors. As we have commented above, we leave the discussion of this to the following section.

Our analytic model, which only employs the real-space $l = 0$ moment as input, reasonably fits the results from simulations. Therefore, it can be used to make forecasts for the precision measuring cosmological parameters from samples with different number densities, linear biases, photo- z errors, and cosmologies. Furthermore, we can use this model to look for the best sample to constrain cosmology. All the above considerations should be taken into account for the optimal design of future galaxy surveys. For instance, the photo- z errors for a given galaxy sample might not only depend on the hardware employed, but also on the intrinsic properties of galaxies (e.g. brighter objects having more accurate redshift estimates). In such case, the sample that delivers the strongest constraints on cosmological parameters is not necessarily the one with the smallest photo- z errors.

6.5 Loss of transverse information from the analysis of power spectrum moments

As we showed in the previous section, for large number densities D_A is measured with more precision from samples with sub-percent photo- z errors than from samples with no errors. We obtain the same results from simulations and from the analytic model introduced in Eq. 33. As the introduction of photo- z errors cannot increase the amount of cosmological information, this highlights that the analysis of power spectrum moments does not extract all the cosmological information encoded in BAO. Therefore, it is worth to follow other approaches such as the analysis of the full anisotropic power spectrum (e.g., Ballinger et al. 1996).

This reduction of the cosmological information available from BAO analyses only appears in redshift space. RSD suppress more strongly parallel k -modes, and when we take the angular average of the power spectrum to compute its moments, we treat in the same way all k -modes, even when the ones parallel to the LOS are noisier. Consequently, the resulting power spectrum obtained after averaging over all k -modes in a k -bin is noisier than if only perpendicular k -modes are considered. For samples with photo- z errors this is not the

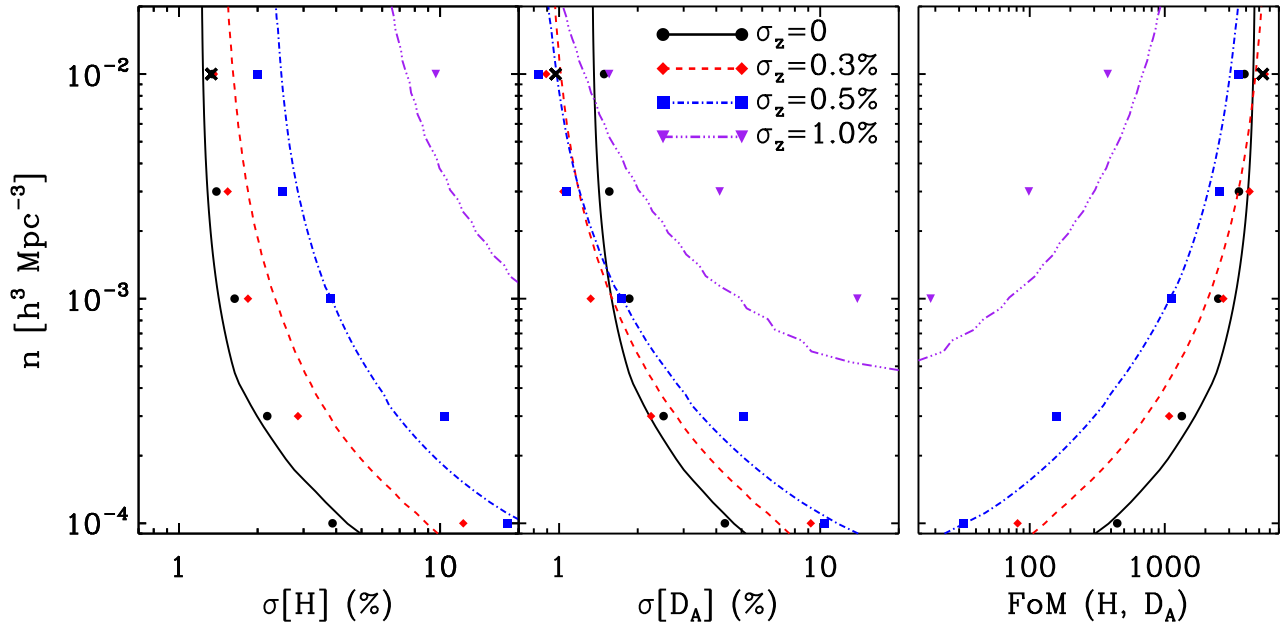


Figure 13. Precision measuring the Hubble parameter (left panel), the angular diameter distance (middle panel), and their FoM from the BAO analysis of samples with different number densities and Gaussian photo- z errors. Each symbols indicate the average result from 1000 samples from the COLA ensemble and the lines show analytic predictions from Eq. 33 using $A_0 = 0.35$, $A_2 = 0.50$, $A_4 = 0.55$, and $c = 0.3$. The uncertainty in H grows with the size of photo- z errors and by decreasing the number density. On the other hand, the behaviour of $\sigma[D_A]$ is more complex, where samples with sub-percent photo- z errors have more precision measuring D_A than samples with no errors. This highlights that all the cosmological information encoded on BAO is not recovered from the analysis of power spectrum moments. Black crosses indicate the results after deconvolving the effect of RSD using Eq. 46 in samples with $10^{-2} h^3 \text{Mpc}^{-3}$ and no photo- z errors. This simple algorithm increases by 54% the precision measuring D_A .

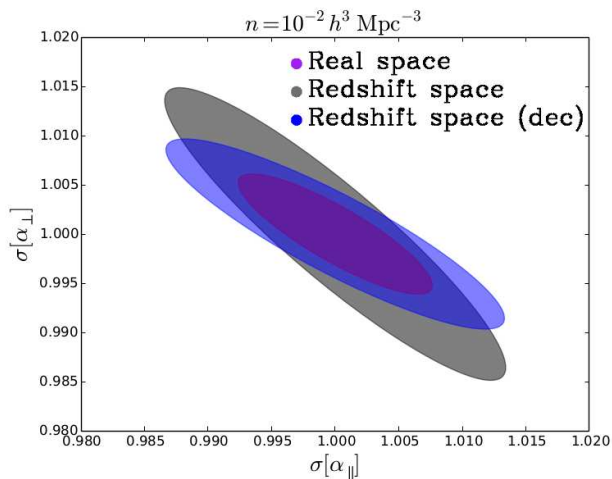


Figure 14. Same as Fig. 12 for samples with $n = 10^{-2} h^3 \text{Mpc}^{-3}$ and no photo- z errors in real space, redshift space, and redshift space after deconvolving the effect of RSD (in purple, grey, and blue, respectively). The strongest constraints on H ($\sigma[\alpha_{\parallel}]$) come from real-space moments because RSD further suppress BAO along the LOS. The constraints on D_A ($\sigma[\alpha_{\perp}]$) should be approximately the same in real- and redshift-space; however, they precision measuring D_A is 2.4 times smaller in redshift space. As we can see, this is partially corrected by the deconvolution procedure introduced in §6.5.

case, as they reduce the weight of parallel k -modes during the angular average, and thus the uncertainty after angular averaging over all k -modes is approximately the same as for perpendicular k modes (c.f. §4.1).

To probe that the angular average of k -modes with different uncertainties causes D_A to be measured with smaller precision, we deconvolve the effect of RSD from power spectrum moments:

$$\tilde{P}(k) = \left\langle \frac{n\hat{P}(k, \mu) - 1}{n\mathcal{F}^2(k, \mu)} \right\rangle_{\hat{\mathbf{k}}} . \quad (46)$$

In Fig. 14 we show the average uncertainty in cosmological parameters computed from 1000 samples of the COLA ensemble with $n = 10^{-2} h^3 \text{Mpc}^{-3}$ and no photo- z errors. The purple, grey, and blue ellipses indicate the results in real space, redshift space, and redshift space after deconvolving the effect of RSD. Our deconvolution procedure increases the precision measuring D_A and the FoM of H and D_A by 54% and 37%, respectively, and, as expected, it does not reduce $\sigma[H]$. Nevertheless, our naive approach does not totally correct the effect of RSD, as real-space power spectrum moments measure H and D_A with greater precision.

We note that Eq. 46 cannot be applied to samples with photo- z errors on intermediate and small scales. This is because they strongly suppress k -modes with $\mu \simeq 1$, which causes them to be completely dominated by shot noise, and our shot noise subtraction is not accurate enough in this regime. Nonetheless, a correct characterisation of shot noise in this regime could lead to a joint deconvolution of RSD and photo-

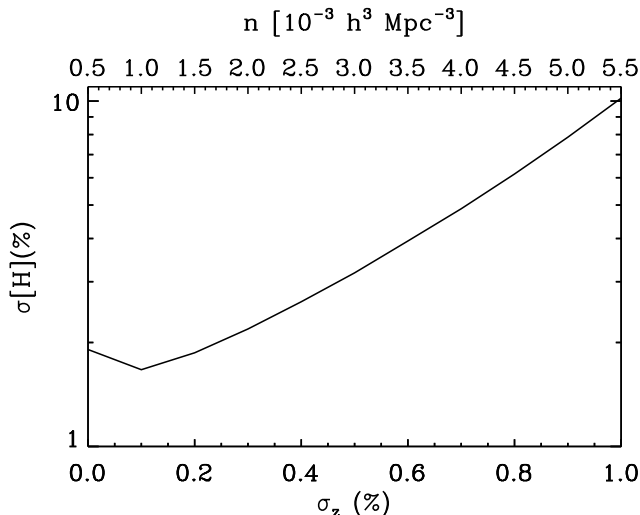


Figure 15. Forecasts for the precision measuring H in spectro-photometric galaxy surveys at $z = 1$. The results are computed assuming a comoving volume of $V = 78.7 \text{ Gpc}^3$ and that the number density of galaxies linearly scales with σ_z . As we can see, galaxy samples with $\sigma_z \leq 0.3\%$ measure the Hubble parameter with approximately the same precision.

z errors. We note that there are other approaches in the literature to reduce the impact of photo- z errors on the power spectrum (e.g., McQuinn & White 2013).

7 FORECASTS FOR FUTURE GALAXY SURVEYS

In §4.3 we introduced an analytic expression to compute the precision measuring cosmological parameters from BAO analyses, and in the previous section we showed that this model approximately reproduces the results from numerical simulations. In this section we use this expression to forecast the precision in H from future spectro-photometric surveys at $z = 1$. We note that the results of this section are illustrative.

In what follows we will assume that the number density of galaxies linearly scale with the size of photo- z errors (see table 8 of Benitez et al. 2014) and that the analysed volume is $V = 78.7 \text{ Gpc}^3$, i.e. the same volume as each COLA simulation. In particular, we take the relation between number density and photo- z errors to be $n = 5(1+10^3\sigma_z)10^{-4} h^3 \text{ Mpc}^{-3}$. In Fig. 15 we display the precision measuring H after marginalising over D_A from galaxy samples with $b = 2$ and different photo- z errors. For samples with $\sigma_z \leq 0.3\%$, the precision measuring H is approximately the same. On the other hand, for $\sigma_z > 0.3\%$ the uncertainty in H is rapidly increased. This encourages the employment of spectroscopic and spectro-photometric surveys with $\sigma_z < 0.5\%$ to study the expansion history of the Universe.

In summary, to design and fully exploit galaxy surveys that employ noisy estimators to compute redshifts, it is necessary to carefully select the properties of the target galaxy sample.

8 CONCLUSIONS

The next generation of galaxy surveys will dramatically increase the precision of measurements for the expansion and growth history of the Universe. Some of these surveys will observe large areas of the sky with linear variable filters or dozens of narrow-bands, providing a low-resolution spectra for every region of the sky. In addition, they will measure the redshift of millions of galaxies with sub-percent accuracy, offering a promising way of constraining cosmological parameters. Nevertheless, to fully exploit this new kind of data it is necessary to fully characterise the effect of photo- z errors on cosmological observables.

In this work we presented a detailed study of the impact of sub-percent photo- z errors on the clustering of galaxies in Fourier space, with an emphasis on the BAO signal. We derived analytic expressions for how photo- z errors modify power spectrum moments, their variances, and the smearing of BAO, which we compared with the results from 1000 N -body simulations.

Our main findings can be summarised as follows:

- In real space photo- z errors suppress power spectrum moments on intermediate and small scales. This increases the interval of scales dominated by shot noise, which reduces the range of scales available for BAO analyses. There is an additional effect in redshift space: the suppression of angular-averaged BAO wiggles gets weaker with increasing photo- z errors. This is because photo- z errors reduce the weight of LOS k -modes in computing power spectrum moments which have more diluted BAO signal due to nonlinear RSD.
- We derived how the cosmological information encoded in BAO depends on the properties of the galaxy sample studied. We showed that small-scale RSD and/or photo- z errors induce a scale-dependence on this information, where the dependence on the Hubble parameter (angular diameter distance) decreases (increases) with the size of photo- z errors.
- Based on these findings, we built a model for extracting cosmological information from the analysis of power spectrum moments. Then, we applied it to simulated galaxy catalogues with different number densities and photo- z errors. We found that photo- z errors do not introduce an additional shift in the position of the BAO scale with respect to the no photo- z error case. Therefore, they do not bias the cosmological information encoded in BAO. In addition, we found that assuming that photo- z errors are Gaussian in BAO analyses, even when they are drawn from PDFs with large excess kurtosis and skewness, does not bias the results.
- In §6.4 we analysed the precision measuring the Hubble parameter and the angular diameter distance from samples with different number densities and photo- z errors. We found that for the same number density, the uncertainty in measuring H decreases with the size of photo- z errors. Nevertheless, it is still possible to measure H with the same (or more) precision from samples with sub-percent photo- z errors as from samples with no errors if the number density of the first is increased. Finally, we also found that the analysis of power spectrum moments artificially decreases the precision in measuring D_A . We suggest to analyse the 2D power spectrum in future studies.

Our results encourage the measurement of cosmological parameters from spectro-photometric surveys, as in general they are deeper than spectroscopic surveys for the same integration time. In §7 we forecast the precision in measuring

the Hubble parameter from BAO analyses assuming that the number density of galaxies linearly scales with the size photo- z errors. Roughly, we found the same results for galaxy samples with redshift uncertainties smaller than $\sigma_z = 0.4\%$. This means that galaxy surveys with sub-percent photo- z errors could set constraints on the dark energy equation of state as precise as spectroscopic surveys.

Along this paper we put a focus on extracting cosmological information from galaxy samples with sub-percent photo- z errors. Recently, Ross et al. (2017) conducted a similar investigation in configuration space for samples with photo- z errors of a few percent, finding that for those the BAO feature mostly constrains $D_A(z)$ and that the projected correlation function is enough for extracting all cosmological information. Their findings agree with ours for samples with $\sigma_z = 1\%$, as we can see in Figs. 12 and 13. Nevertheless, as we show along this work, for samples with smaller photo- z errors $H(z)$ can be constrained from the 3D galaxy clustering.

Finally, our paper highlights that photo- z errors substantially increase the complexity of the extraction of cosmological information from BAO analyses. Therefore, it is crucial a thorough understanding and modelling of photo- z errors in galaxy clustering. We hope our work to have clarified some the most important aspects of this issue, and that it will help in the cosmological analysis of future spectro-photometric surveys.

ACKNOWLEDGEMENTS

We thank the anonymous referee for the thorough review, insightful comments, and positive suggestions. We acknowledge discussions with Raul Abramo, Andreu Font-Ribera, Licia Verde, and Carlos López-Sanjuan. Argonne National Laboratory's work was supported by the U.S. Department of Energy, Office of Science, Office of Nuclear Physics, under contract DE-AC02-06CH11357. The authors acknowledge support from the Spanish Ministry of Economy and Competitiveness (MINECO) through the project AYA2015-66211-C2-2. JCM acknowledges support from the Fundación Bancaria Ibercaja for developing this research. REA acknowledges support from the European Research Council through grant number ERC-StG/716151. CHM acknowledges support from the Ramon y Cajal Fellow Program of the Spanish MINECO. This project has received funding from the European Unions Horizon 2020 Research and Innovation Programme under the Marie Skłodowska-Curie grant agreement No 734374.

REFERENCES

- Abramowitz M., Stegun I. A., 1972, Handbook of Mathematical Functions
- Alcock C., Paczynski B., 1979, *Nature*, 281, 358
- Angulo R. E., Baugh C. M., Frenk C. S., Lacey C. G., 2008, *MNRAS*, 383, 755
- Angulo R. E., Pontzen A., 2016, *MNRAS*, 462, L1
- Angulo R. E., Springel V., White S. D. M., Jenkins A., Baugh C. M., Frenk C. S., 2012, *MNRAS*, 426, 2046
- Angulo R. E., White S. D. M., Springel V., Henriques B., 2014, *MNRAS*, 442, 2131
- Ballinger W. E., Peacock J. A., Heavens A. F., 1996, *MNRAS*, 282, 877
- Benítez N. et al., 2014, ArXiv e-prints
- Benítez N. et al., 2009, *ApJ*, 691, 241
- Bjerhammar A., 1951, *Trans. Roy. Inst. Tech. Stockholm*, 1951, 86 pp. (2 plates)
- Blake C., Bridle S., 2005, *MNRAS*, 363, 1329
- Cai Y.-C., Angulo R. E., Baugh C. M., Cole S., Frenk C. S., Jenkins A., 2009, *MNRAS*, 395, 1185
- Chaves-Montero J. et al., 2017, *MNRAS*, 472, 2085
- Colombi S., Jaffe A., Novikov D., Pichon C., 2009, *MNRAS*, 393, 511
- Crocce M., Scoccimarro R., 2008, *Phys. Rev. D*, 77, 023533
- Dalton G. et al., 2014, in *Proc. SPIE*, Vol. 9147, Ground-based and Airborne Instrumentation for Astronomy V, p. 91470L
- de Jong R., 2011, *The Messenger*, 145, 14
- DESI Collaboration et al., 2016, ArXiv e-prints
- Dolney D., Jain B., Takada M., 2006, *MNRAS*, 366, 884
- Doré O. et al., 2014, ArXiv e-prints
- Doré O. et al., 2016, ArXiv e-prints
- Eisenstein D. J., Hu W., 1998, *ApJ*, 496, 605
- Eisenstein D. J., Seo H.-J., Sirko E., Spergel D. N., 2007, *ApJ*, 664, 675
- Eisenstein D. J. et al., 2005, *ApJ*, 633, 560
- Foreman-Mackey D., Hogg D. W., Lang D., Goodman J., 2013, *PASP*, 125, 306
- Glazebrook K., Blake C., 2005, *ApJ*, 631, 1
- Hartlap J., Simon P., Schneider P., 2007, *A&A*, 464, 399
- Hockney R. W., Eastwood J. W., 1981, *Computer Simulation Using Particles*
- Howlett C., Manera M., Percival W. J., 2015, *Astronomy and Computing*, 12, 109
- Ilbert O. et al., 2009, *ApJ*, 690, 1236
- Kaiser N., 1987, *MNRAS*, 227, 1
- Kashlinsky A., Hernández-Monteagudo C., Atrio-Barandela F., 2001, *ApJ*, 557, L1
- Koda J., Blake C., Beutler F., Kazin E., Marin F., 2016, *MNRAS*, 459, 2118
- Laureijs R. et al., 2011, ArXiv e-prints
- Lidz A., Taylor J., 2016, *ApJ*, 825, 143
- Martí P., Miquel R., Castander F. J., Gaztañaga E., Eriksen M., Sánchez C., 2014, *MNRAS*, 442, 92
- McQuinn M., White M., 2013, *MNRAS*, 433, 2857
- Moore R. L., 1920, *Bull. Amer. Math. Soc.*, 26, 412
- Orsi A. A., Angulo R. E., 2017, ArXiv e-prints
- Padmanabhan N., White M., 2008, *Phys. Rev. D*, 77, 123540
- Padmanabhan N., White M., 2009, *Phys. Rev. D*, 80, 063508
- Peacock J. A., Dodds S. J., 1994, *MNRAS*, 267, 1020
- Penrose R., 1955, *Proc. Cambridge Philos. Soc.*, 51, 406
- Ross A. J. et al., 2017, ArXiv e-prints
- Ross A. J., Percival W. J., Manera M., 2015, *MNRAS*, 451, 1331
- Sánchez A. G., Baugh C. M., Angulo R. E., 2008, *MNRAS*, 390, 1470
- Schmittfull M., Feng Y., Beutler F., Sherwin B., Chu M. Y., 2015, *Phys. Rev. D*, 92, 123522
- Scoccimarro R., 2004, *Phys. Rev. D*, 70, 083007
- Sefusatti E., Crocce M., Scoccimarro R., Couchman H. M. P., 2016, *MNRAS*, 460, 3624
- Seo H.-J., Eisenstein D. J., 2003, *ApJ*, 598, 720
- Seo H.-J., Eisenstein D. J., 2007, *ApJ*, 665, 14
- Sereno M., Veropalumbo A., Marulli F., Covone G., Moscardini L., Cimatti A., 2015, *MNRAS*, 449, 4147
- Smith R. E., Scoccimarro R., Sheth R. K., 2008, *Phys. Rev. D*, 77, 043525
- Szapudi I., Prunet S., Pogosyan D., Szalay A. S., Bond J. R.,

2001, ApJ, 548, L115

Tassev S., Zaldarriaga M., Eisenstein D. J., 2013, JCAP, 6, 036

Weinberg D. H., Mortonson M. J., Eisenstein D. J., Hirata C., Riess A. G., Rozo E., 2013, Phys. Rep., 530, 87

Xu X., Cuesta A. J., Padmanabhan N., Eisenstein D. J., McBride C. K., 2013, MNRAS, 431, 2834